

## Alert Classification for the ALerCE Broker System: The Light Curve Classifier

P. SÁNCHEZ-SÁEZ,<sup>1,2,3</sup> I. REYES,<sup>1,4,5</sup> C. VALENZUELA,<sup>4,1</sup> F. FÖRSTER,<sup>6,1,7</sup> S. EYHERAMENDY,<sup>3,1</sup> F. ELORRIETA,<sup>6,1</sup>  
F. E. BAUER,<sup>2,8,1,9</sup> G. CABRERA-VIVES,<sup>10,1</sup> P. A. ESTÉVEZ,<sup>5,1</sup> M. CATELAN,<sup>2,8,1</sup> G. PIGNATA,<sup>11,1</sup> P. HUIJSE,<sup>12,1</sup>  
D. DE CICCIO,<sup>1,2</sup> P. ARÉVALO,<sup>13</sup> R. CARRASCO-DAVIS,<sup>5</sup> J. ABRIL,<sup>14,15</sup> R. KURTEV,<sup>13,1</sup> J. BORISSOVA,<sup>13,1</sup> J. ARREDONDO,<sup>1</sup>  
E. CASTILLO-NAVARRETE,<sup>1,4</sup> D. RODRIGUEZ,<sup>1</sup> D. RUZ-MIERES,<sup>1,4</sup> A. MOYA,<sup>4,1</sup> L. SABATINI-GACITÚA,<sup>4,1</sup> AND  
C. SEPÚLVEDA-COBO<sup>4,1</sup>

<sup>1</sup>*Millennium Institute of Astrophysics (MAS), Nuncio Monseñor Sótero Sanz 100, Providencia, Santiago, Chile*

<sup>2</sup>*Instituto de Astrofísica, Facultad de Física, Pontificia Universidad Católica de Chile, Casilla 306, Santiago 22, Chile*

<sup>3</sup>*Faculty of Engineering and Sciences, Universidad Adolfo Ibáñez, Diagonal Las Torres 2700, Peñalolén, Santiago, Chile*

<sup>4</sup>*Center for Mathematical Modeling, Universidad de Chile, Beauchef 851, North building, 7th floor, Santiago 8320000, Chile*

<sup>5</sup>*Department of Electrical Engineering, Universidad de Chile, Av. Tupper 2007, Santiago 8320000, Chile*

<sup>6</sup>*Departamento de Matemáticas, Facultad de Ciencia, Universidad de Santiago de Chile, Av. Libertador Bernardo O'Higgins 3663, Estación Central, Santiago, Chile*

<sup>7</sup>*Departamento de Astronomía, Universidad de Chile, Casilla 36D, Santiago, Chile*

<sup>8</sup>*Centro de Astroingeniería, Pontificia Universidad Católica de Chile, Av. Vicuña Mackenna 4860, 7820436 Macul, Santiago, Chile*

<sup>9</sup>*Space Science Institute, 4750 Walnut Street, Suite 205, Boulder, Colorado 80301*

<sup>10</sup>*Department of Computer Science, University of Concepción, Edmundo Larenas 219, Concepción, Chile*

<sup>11</sup>*Departamento de Ciencias Físicas, Universidad Andres Bello, Auda. Republica 252, Santiago, Chile*

<sup>12</sup>*Informatics Institute, Universidad Austral de Chile, General Lagos 2086, Valdivia, Chile*

<sup>13</sup>*Instituto de Física y Astronomía, Facultad de Ciencias, Universidad de Valparaíso, Gran Bretaña No. 1111, Playa Ancha, Valparaíso, Chile*

<sup>14</sup>*European Southern Observatory (ESO), Alonso de Córdova 3107, Vitacura, Santiago, Chile*

<sup>15</sup>*Centro de Estudios de Física del Cosmos de Aragón (CEFCA) - Unidad Asociada al CSIC, Plaza San Juan, 1, E-44001, Teruel, Spain*

(Received; Revised; Accepted)

Submitted to AJ

### ABSTRACT

We present the first version of the ALerCE (Automatic Learning for the Rapid Classification of Events) broker light curve classifier. ALerCE is currently processing the Zwicky Transient Facility (ZTF) alert stream, in preparation for the Vera C. Rubin Observatory. The ALerCE light curve classifier uses variability features computed from the ZTF alert stream, and colors obtained from AllWISE and ZTF photometry. We apply a Balanced Hierarchical Random Forest algorithm with a two-level scheme, where the top level classifies each source as periodic, stochastic, or transient, and the bottom level further resolve each hierarchical class, yielding a total of 15 classes. This classifier corresponds to the first attempt to classify multiple classes of stochastic variables (including nucleus- and host-dominated active galactic nuclei, blazars, young stellar objects, and cataclysmic variables) in addition to different classes of periodic and transient sources, using real data. We created a labeled set using various public catalogs (such as the Catalina Surveys and *Gaia* DR2 variable stars catalogs, and the Million Quasars catalog), and we classify all objects with  $\geq 6$  *g*-band or  $\geq 6$  *r*-band detections in ZTF (868,371 sources as of 2020/06/09), providing updated classifications for sources with new alerts every day. For the top level we obtain macro-averaged precision and recall scores of 0.96 and 0.99, respectively, and for the bottom level we obtain macro-averaged precision and recall scores of 0.57 and 0.76, respectively. Updated classifications from the light curve classifier can be found at the [ALerCE Explorer website](#).

*Keywords:* galaxies: active – methods: data analysis – stars: variables: general – supernovae: general  
– surveys

## 1. INTRODUCTION

Brightness variations of astrophysical objects offer key insights into their physical emission mechanisms and related phenomena. In stars, pulsations, both radial and non-radial, can result from a thermodynamic engine operating in their partial ionization layers, when stars are located inside one of the several so-called instability strips that are found in the Hertzsprung-Russell diagram. Eruptive events can be generated by material being lost from a star, or occasionally accreted onto it, as is typical in protostars and young stellar objects (YSOs). Explosive events can occur when material is accreted onto compact objects, such as white dwarfs in the case of cataclysmic variables (CVs) or neutron stars in the case of X-ray binaries, or star mergers. Brightness changes can also originate from the rotation of stars, caused by surface features such as starspots, and/or by stars’ ellipsoidal shapes. Finally, eclipses can occur, depending on the observer’s line-of-sight, due to the presence of binary companions, planets, and/or other circumstellar material. These and other classes of stellar variability are reviewed and summarized, for instance, in [Catelan & Smith \(2015\)](#), where extensive additional references can be found. In addition, there are a wide array of transients such as kilonovae ([Metzger et al. 2010](#)), supernovae (SNe; [Woosley et al. 2002](#)), and tidal disruption events, which are beacons of destructive episodes in the life of a star ([Komossa 2015](#)). Galaxies, in turn, can also present a wide array of variability phenomena. In those hosting strongly accreting massive black holes (BHs), for instance, variations develop due to the stochastic nature of the accretion disk, corona, and jet emission, potentially related to both the BH properties and the structure of the material in the immediate vicinity (e.g., [MacLeod et al. 2010](#); [Caplar et al. 2017](#); [Sánchez-Sáez et al. 2018](#)).

To study the variability of individual variable and transient objects in detail, and to use this information to probe different variability and physical models, observations over a wide range of timescales are required. Hence, long and intensive campaigns of a large number of targets are crucial. In recent years surveys covering a significant part of the sky, revisiting the same regions on timescales from days to years, and containing a large sample of serendipitous objects, are now becoming available as predecessors of the Vera C. Rubin Observatory Legacy Survey of Space and Time (LSST; [Ivezić et al. 2019](#)).

Among these is the Zwicky Transient Facility (ZTF; [Bellm 2014](#); [Bellm et al. 2019](#)), which had first light in 2017 and employs a powerful 47 deg<sup>2</sup> field-of-view camera mounted on the Samuel Oschin 48-inch Schmidt telescope. ZTF is designed to image the entire northern sky every three nights and scan the plane of the Milky Way twice each night to a limiting magnitude of 20.5 in *gri*, thus enabling a wide variety of novel multiband time series studies, in preparation for the LSST.

LSST, which aims for first light in 2022, will revolutionize time domain astronomy, enabling for the first time the study of transient and variable objects over long periods of time ( $\sim 10$  years) with  $\gtrsim 1000$  visits, down to very faint magnitudes ( $r \sim 24.5$  for single images of the entire sky every 3 days,  $\sim 26.1$  for yearly stacks, and  $\sim 27.5$  at full depth;  $5\sigma$ ), over a large sky area ( $>18,000$  deg<sup>2</sup>).

Given the large number of sources that ZTF and LSST will observe ( $\sim 1\text{--}40$  billion objects), it is critical to develop reliable and efficient variability-based selection techniques. This new information allows us to see through degeneracies which might exist from color characterization alone. These selection techniques should ideally take advantage of the multiband light curves provided by surveys like LSST and ZTF, and separate different subclasses of variable and transient objects without the need for optical spectra, which are still quite expensive to obtain for such large samples.

This new generation of large etendue survey telescopes has demonstrated a growing need for sophisticated astronomical alert processing systems (i.e., systems that are able to detect changes in the sky of an astrophysical origin). These systems involve the real-time processing of data for alert generation, real-time annotation and classification of alerts (up to 40 million events per night) and real-time reaction to interesting alerts using available astronomical resources (e.g., via Target Observation Managers, or TOMs). In order to use these resources intelligently and efficiently, the astronomical community has been developing a new generation of alert filtering systems known as “brokers”. One such community broker is the project ALerCE (Automatic Learning for the Rapid Classification of Events; [Förster 2020](#)). ALerCE is an initiative led by an interdisciplinary and inter-institutional group of scientists from several institutions both in Chile and the United States. The main aim of ALerCE is to facilitate the study of non-moving variable and transient objects.

ALeRCE is currently processing the ZTF alert stream, providing classifications of different variable and transient objects, in preparation for the LSST era. Two classification models are currently available in the ALeRCE pipeline: a stamp classifier (or early classifier; Carrasco-Davis 2020), that uses a Convolutional Neural Network on the first detection stamp of a source to classify it among five broad classes, namely variable star, active galactic nuclei, SN, asteroid, or bogus; and a light curve classifier (or late classifier), that uses variability features computed from the light curves to classify each source into finer (currently 15) subclasses among three of the five broad classes.

In this work we present the first version of the ALeRCE light curve classifier. This classifier uses several novel features (see Section 3), and employs machine learning (ML) algorithms that can deal with the high class imbalance present in the data. A key goal of ALeRCE is to provide fast classification of transient and variable objects in a highly scalable framework, and thus we only include in this model features that can be computed quickly, avoiding features that require more than one second to compute, based on the computational infrastructure currently at our disposal (see Förster 2020). The main advantage of this classifier is that it can separate multiple classes of transient and persistent variable objects, using features computed from real data, that would be measured from LSST data. Particularly, the light curve classifier can deal with multiple classes of stochastic variable objects (including nucleus, host, and jet dominated active galactic nuclei, YSOs, and CVs), which have been normally not included by previous classifiers that use real data and classify periodic and transient objects (e.g., Richards et al. 2009; Kim et al. 2014; Nun et al. 2016; Villar et al. 2019a).

This work attempts to separate an unprecedentedly large number of classes (15) of both transients and persistent variable objects using real data (as opposed to using only simulated data). Previous works using real data have mostly focused on selecting either a variety of variable stars classes (e.g., Debosscher et al. 2009; Richards et al. 2012; Kim & Bailer-Jones 2016; Elorrieta et al. 2016; Rimoldini et al. 2019; Zorich et al. 2020), different classes of variable objects, including variable stars and active galactic nuclei (e.g., Kim et al. 2014; Nun et al. 2016), or different classes of transients (Villar et al. 2019a).

To the best of our knowledge three previous works have used real data to classify transients and persistent variable objects, albeit considering a lower number of classes: Martínez-Palomera et al. (2018) used data from the HiTS survey (Förster et al. 2016, 2018) to classify

eight transient, active galactic nuclei and variable star classes; Narayan et al. (2018) used data from The Optical Gravitational Lensing Experiment (OGLE; Udalski et al. 1992) and the Open Supernova Catalog (OSC; Guillochon et al. 2017) to classify seven transient and variable star classes; and D’Isanto et al. (2016) used Catalina Real-Time Transient Survey (CRTS; Drake et al. 2009) data to classify six transient and variable object classes. Other works have tested techniques to classify different classes of variables and transients using synthetic data (e.g., Boone 2019), or a combination of synthetic and real data (e.g., Carrasco-Davis et al. 2019).

In addition, this work is the first attempt to separate three different classes of active galactic nuclei (nucleus-dominated or quasi-stellar objects, hereafter “QSO”; host-dominated, hereafter “AGN”; and jet-dominated, hereafter “Blazar”). Previous works have mostly focused on separating active galactic nuclei from the rest (e.g., Butler & Bloom 2011; Peters et al. 2015; Palanque-Delabrouille et al. 2016; Sánchez-Sáez et al. 2019; De Cicco et al. 2019).

The paper is organized as follows. In Section 2 we describe the data used for this work, the procedure for the light curve construction, as well as the taxonomy and the labeled set used to train the classifier. In Section 3 we define the set of features used by the light curve classifier. In Section 4 we describe the different ML algorithms tested for the classifier. In Section 5 we compare the performance of the different models, and report the results obtained for the labeled and unlabeled ZTF sets. Finally in Section 6 we summarize the paper, provide conclusions, and discuss the challenges found during the development of the classifier and the future work.

## 2. DATA

### 2.1. Reference Data

ALeRCE has been processing the public ZTF alert stream since May 2019, which includes  $g$  and  $r$  photometry. The ALeRCE pipeline is described in detail by Förster (2020); for clarity, we provide a brief description of the light curve construction process.

The ALeRCE pipeline processes the ZTF Avro alert files.<sup>1</sup> These files contain metadata and contextual information for a single event, which are defined as a flux-transient, a reoccurring flux-variable, or a moving object (Masci et al. 2019). To construct light curves, the ALeRCE pipeline uses: the photometry of

<sup>1</sup> For details, see <https://zwickyttransientfacility.github.io/ztf-avro-alert/>.

the difference-image and reference-image (detections); possible non-detections associated with the target during the previous 30 days of the event ( $5\sigma$  magnitude limit in the difference image based on PSF-fit photometry, called `diffmaglim` by ZTF); the real-bogus quality score reported by ZTF (`rb`, which ranges from 0 to 1, with values closer to 1 implying more reliable detections); and the morphological classification of the closest object obtained from PanSTARRS1 (Tachibana & Miller 2018). An overview of the pipeline is presented in Figure 1. In addition, Figure 2 shows an example of a SN light curve obtained using ZTF data. In summary, the different stages of the pipeline are:

- 1) Ingestion: the ZTF public stream is ingested using Kafka.
- 2) S3 upload: the alert Avro packets are stored in AWS S3 for later access.
- 3) Crossmatch: the position of the alert is used to query external catalogs.
- 4) Stamp classifier: alerts from new objects are classified using their image cutouts (stamps).
- 5) Preprocessing: the photometry associated with a given alert is corrected to take into account the use of difference image fluxes (see details below), and simple statistics associated with the aggregated light curve are computed.
- 6) Light curve features: advanced light curve statistics (features) are computed when there are at least six detections in a given band.
- 7) Light curve classifier: the light curve classifier described in this work is applied.
- 8) Outliers: an outlier detection algorithm is applied.
- 9) ALerCE stream: the aggregated, annotated and classified light curves are reported in a Kafka stream.

In step 3) we are experimenting with several catalogs, but for this work we use the AllWISE<sup>2</sup> public Source Catalog (Wright et al. 2010; Mainzer et al. 2011), invoking a match radius of 2 arcseconds, to obtain W1, W2, and W3 photometry (using magnitudes measured with profile-fitting photometry, e.g., `wlmp`).

The preprocessing procedure (step 5) is described in detail in Förster (2020) (see Section A of their appendix). In particular, for the light curve classifier we

use the corrected light curves (`lc_corr`;  $\hat{m}_{\text{sci}}$  in Förster 2020) for sources whose closest source in the reference image coincides with the location of the alert (in a radius of 1.4 arcseconds). It is important to use the corrected light curves for persistent variable sources, in order to take into account changes in the sign of the difference between the reference and the science images, or possible changes of the reference image. For the rest of the sources we use the light curves obtained using the difference images (`lc_diff`;  $m_{\text{diff}}$  in Förster 2020), which correspond in general to transient sources.

## 2.2. Classification Taxonomy

The first version of the ALerCE light curve classifier considers 15 subclasses of variable and transient objects, presented as a taxonomy tree defined by the ALerCE collaboration in Figure 3. The taxonomy is subdivided in a hierarchical fashion according to both the physical properties of each class and the empirical variability properties of the light curves, as follows (in parenthesis we indicate the class name used by the classifier):

- Transient: Type Ia supernova (SNIa), Type Ibc supernova (SNIbc), Type II supernova (SNII), and Super Luminous Supernova (SLSN);
- Stochastic: Type 1 Seyfert galaxy (AGN; i.e., host-dominated active galactic nuclei), Type 1 Quasar (QSO; i.e., nucleus-dominated active galactic nuclei), blazar (Blazar; i.e., beamed jet-dominated active galactic nuclei), Young Stellar Object (YSO), and Cataclysmic Variable/Nova (CV/Nova);
- Periodic: Long-Period Variable (LPV; includes regular, semi-regular, and irregular variable stars), RR Lyrae (RRL), Cepheid (CEP), eclipsing binary (E),  $\delta$  Scuti (DSCT), and other periodic variable stars (Periodic-Other; this includes classes of variable stars that are not well represented in the labeled set, e.g., sources classified as Hump, Misc, Rotational, or RS CVn in CRTS).

It is important to note that there are a number of less common classes which have not been separated out yet in the ALerCE taxonomy tree, because the number of cross-matched objects in these classes is too low to train a good classification model (e.g. SNe IIb, TDEs, KNe, among others). There is a catch-all “Periodic-Other” class for periodic classes excluded in the taxonomy tree, but not for transient or stochastic classes, and thus, for the moment, these missing classes are being grouped into one or more of the existing ones.

<sup>2</sup> <http://wise2.ipac.caltech.edu/docs/release/allwise/>

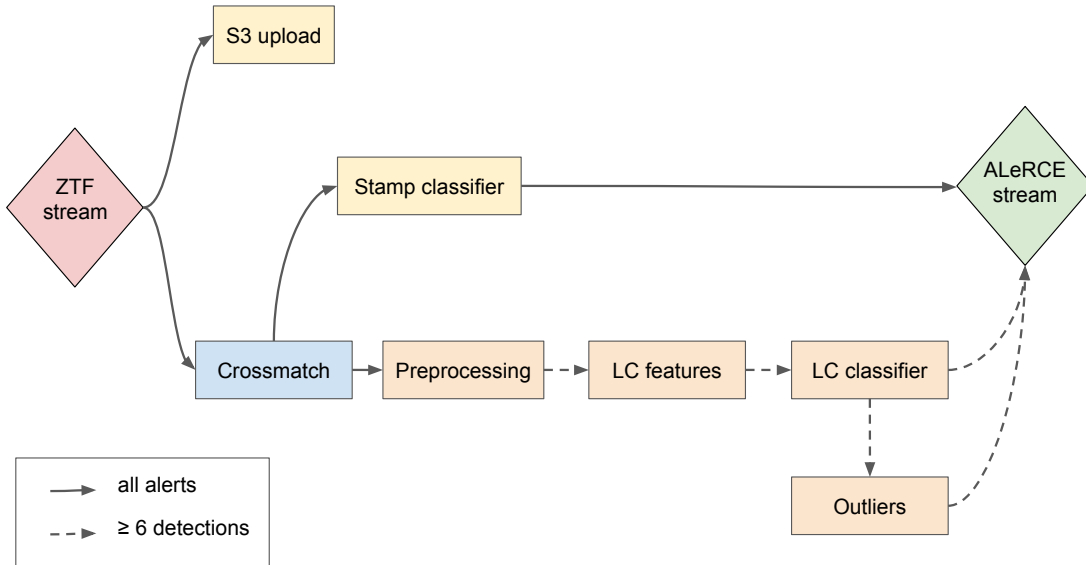


**Figure 1.** A scheme of the ALERCE pipeline. ZTF alerts are ingested using Kafka and a series of sequential and parallel steps are initiated. Alerts are stored in AWS S3, classified based on its image stamps, crossmatched with other catalogs, and their photometry corrected to take into account difference fluxes. Aggregated light curves are used to compute basic statistics (for internal use) and, if enough data points exist, features are computed, and a light curve and outlier classifiers are applied before sending an output stream. A PostgreSQL database is populated along the way, which can then be queried.

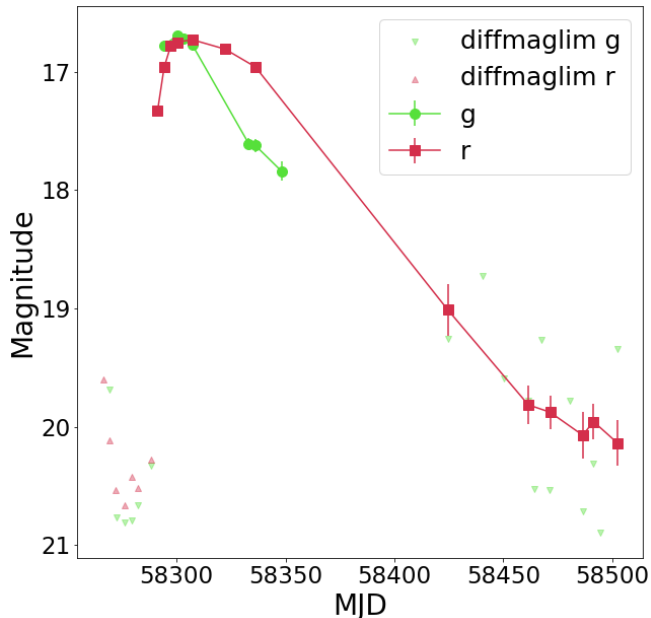


**Figure 2.** A SN light curve queried from the previously populated database (after stage 5 of the pipeline is performed). Green circles and red squares indicate the  $g$  and  $r$  bands, respectively. Error bars indicate photometry associated with detections, with consecutive measurements connected by straight solid line segments. Triangles denote limiting magnitudes.

### 2.2.1. Labeled Set

The labeled set (i.e., the set of sources used to define the training and testing sets) for the light curve classifier was built using sources observed by ZTF with known labels obtained via spectroscopic and/or photometric analysis by previous works. Further description of the labeled set construction strategy can be found in Förster (2020). We obtained labels from the following catalogs: the ASASSN catalogue of variable stars (ASASSN; Jayasinghe et al. 2018, 2019a,b, 2020), the Catalina Surveys Variable Star Catalogs (CRTS; Drake et al. 2014; Drake et al. 2017), LINEAR catalog of periodic light curves (LINEAR; Palaversa et al. 2013), Gaia Data Release 2 (*Gaia*DR2; Mowlavi et al. 2018; Rimoldini et al. 2019), the Transient Name Server database (TNS)<sup>3</sup>, the Roma-BZCAT Multi-Frequency Catalog of Blazars (ROMABZCAT; Massaro et al. 2015), the Million Quasars Catalog (MILLIQUAS, version 6.4c, December 2019; Flesch 2015, 2019), the New Catalog of Type 1 AGNs (Oh2015; Oh et al. 2015), and the SIMBAD database (Wenger et al. 2000). Some additional CV labels were obtained from different catalogs (including Ritter & Kolb 2003), compiled by Abril et al. (2020) (JAbril).

<sup>3</sup> <https://wis-tns.weizmann.ac.il/>

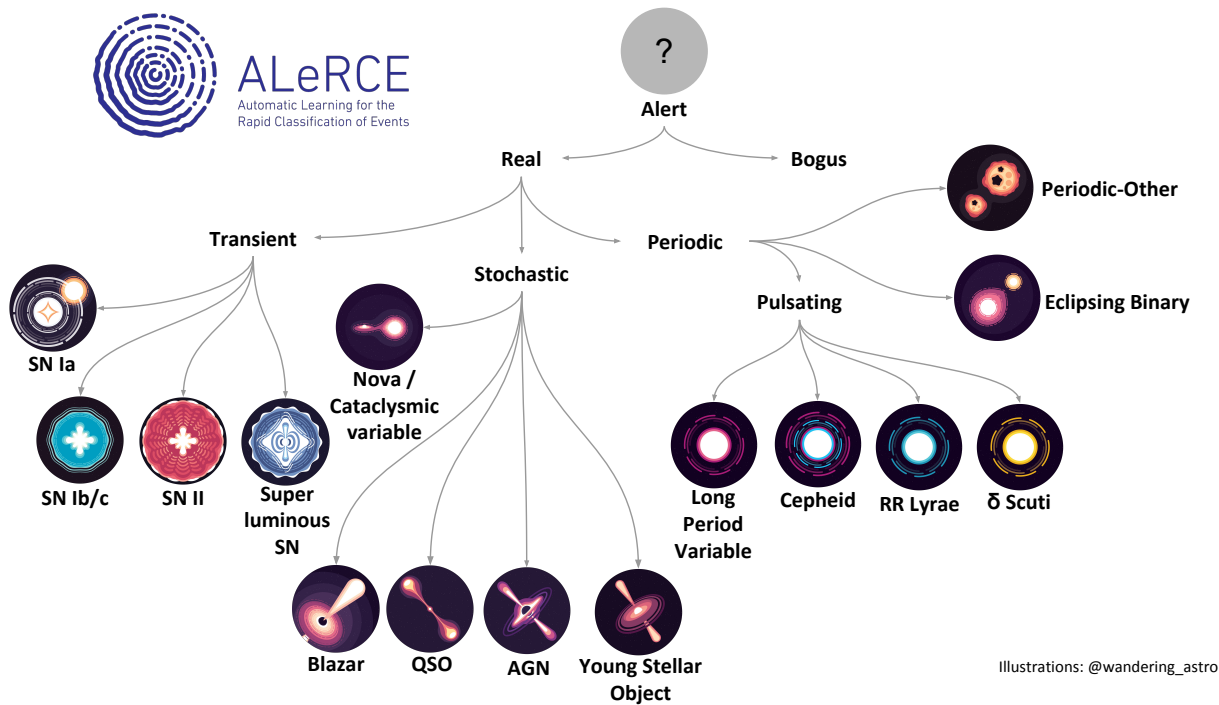


**Figure 3.** Taxonomy tree used in the current version of the ALeRCE light curve classifier.

Table 1 lists the number of sources in the labeled set belonging to each class (with their correspondent percentages according to their hierarchical group), and the catalogs from which the classifications were obtained. Only sources with  $\geq 6$  detections in  $g$  or  $\geq 6$  detections in  $r$  were included (considering data obtained until 2020/06/09). It is clear from the table that there is a high imbalance in the labeled set, with some classes representing less than 5% of their respective hierarchical group. Figure 4 shows the (ordered) number of sources per class for the labeled set, and Figure 5 shows the fraction of sources in each class with photometry only in the  $g$  band, only in the  $r$  band, or in both bands.

### 3. FEATURES USED BY THE CLASSIFIER

The light curve classifier uses a total of 152 features. We avoid including features that require a long time to compute, for example features that require the use of Markov chain Monte Carlo techniques, since one of the goals of the light curve classifier is to provide a fast and highly scalable classification. 146 of these features are computed using the public ZTF  $g$  and  $r$  data. We excluded the mean magnitude as a feature to avoid that any bias in the labeled set magnitude distribution affects the classification of sources that are fainter (or brighter). Features obtained using the ZTF observed magnitudes are called detection features (124 in total),

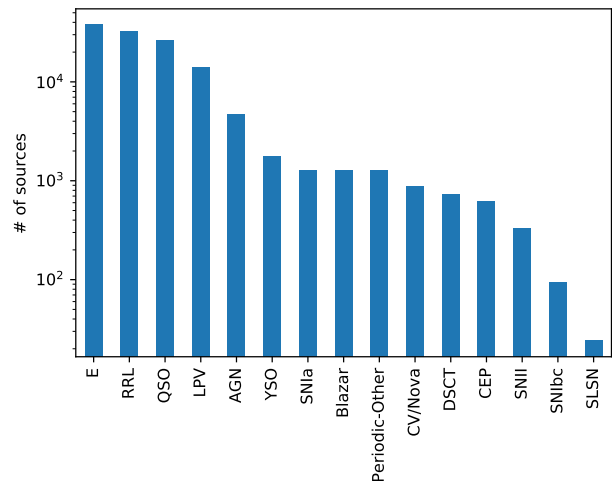


**Figure 4.** Number of sources per class for the labeled set, as reported in Table 1.

and features computed using the ZTF non-detection  $5\sigma$  magnitude limits `diffmaglim`'s are called non-detection features (18 in total). These features are described in the following sections (3.1 and 3.2), as well as in Appendix A. Considering the LSST Data Products Definition Document (Jurić et al. 2019), we expect that all these features would be measured using LSST data.

**Table 1.** Labeled set definition

Hierarchical Class	Class	# of sources <sup>†</sup>	Source Catalogs
Transient	SNIa	1272 (74.0%)	TNS
	SNIbc	94 (5.5%)	TNS
	SNI	328 (19.1%)	TNS
	SLSN	24 (1.4%)	TNS
	Total	1718	
Stochastic	QSO	26168 (75.4%)	MILLIQUAS (sources with class “Q”)
	AGN	4667 (13.4%)	Oh2015, MILLIQUAS (sources with class “A”)
	Blazar	1267 (3.6%)	ROMABZCAT, MILLIQUAS (sources with class “B”)
	YSO	1740 (5.0%)	SIMBAD
	CV/Nova	871 (2.5%)	TNS, ASASSN, JAbriI
Total	34713		
Periodic	LPV	14076 (16.2%)	CRTS, ASASSN, <i>Gaia</i> DR2
	E	37901 (43.5%)	CRTS, ASASSN, LINEAR
	DSCT	732 (0.8%)	CRTS, ASASSN, LINEAR, <i>Gaia</i> DR2
	RRL	32482 (37.3%)	CRTS, ASASSN, LINEAR, <i>Gaia</i> DR2
	CEP	618 (0.7%)	CRTS, ASASSN
	Periodic-Other	1256 (1.4%)	CRTS, LINEAR
	Total	87065	

<sup>†</sup> Values in parentheses correspond to the fraction of sources of a given class (second column) within its corresponding hierarchical class (first column).

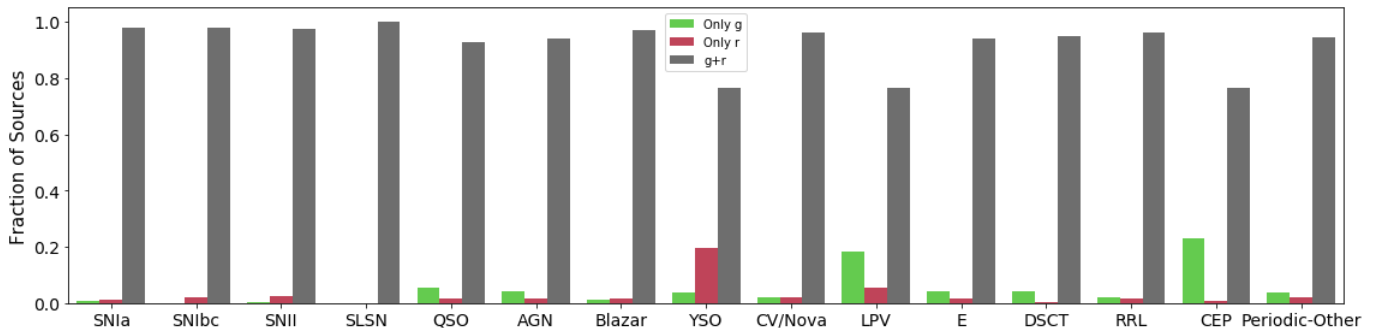


**Figure 5.** For the sources in the labeled set, this figure shows the fraction of sources in each class with photometry: only in the  $g$  band (green); only in the  $r$  band (red); or in both bands (grey). The reasons for the non-uniformity of coverage may be physical (strongly red or blue source) or organizational (survey focused on one band only). For most classes, the vast majority of the sources ( $\gtrsim 92\%$ ) have photometric detections in both  $g$  and  $r$ ; the exceptions are the YSO, LPV, and CEP classes, where only 76% of the sources have photometry in both bands.

We also included as features the galactic coordinates of each target (`gal_b` and `gal_l`), the W1–W2 and W2–W3 AllWISE colors, and the  $g$ –W2,  $g$ –W3,  $r$ –W2, and  $r$ –W3 colors, where  $g$  and  $r$  are computed as the mean magnitude of the  $g$  band and  $r$  band light curves for a given source. In addition, we use information included in the Avro files metadata: the `sgscore1` parameter, which corresponds to a morphological star/galaxy score of the closest source from PanSTARRS1 (Tachibana & Miller 2018) reported in the ZTF Avro files, with  $0 \leq \text{sgscore1} \leq 1$ , where values closer to 1 imply a

higher likelihood of the source being a star; and the median `rb` (real-bogus) parameter for each band.

As we mentioned in Section 2.1, in this work we only consider light curves with  $\geq 6$  epochs in  $g$  or  $\geq 6$  epochs in  $r$ . If a given source has  $\geq 6$  epochs just in one band, it is included in the analysis, and the features associated with the missing band are considered as -999 values. This rule applies to all the features used by the classifier; whenever a feature is not available for a given target, we assume a value equal to -999.

### 3.1. Detection Features

Most of the features used by the light curve classifier are computed using the observed magnitudes in the  $g$  and  $r$  bands (i.e., the detections). There are 56 different features computed for each band, and 12 features computed using a combination of both bands, yielding a total of 124 detection features. The definition of all these features can be found in Table 2. We split the table in three blocks. The first block contains new features defined by this work (i.e., novel features). Some of

these features are further described in Section 3.1.1. The second block contains features that correspond to new variants of descriptors included in other works. Some of them are further described in Section 3.1.1 and in Appendix A. Finally, the third block includes 22 features that come from the Feature Analysis for Time Series (FATS; Nun et al. 2015) Python package. Hereafter, features ending with “\_1” are computed for the  $g$  band, and features ending with “\_2” are computed for the  $r$  band, following the notation used in the ZTF Avro files.

**Table 2.** List of detection features used by the light curve classifier. Features marked with  $\blacklozenge$  are computed using both  $g$  and  $r$  bands at the same time. Features marked with \* and \*\* are further described in Section 3.1.1 and Appendix A, respectively.

Feature	Description	Reference
<code>delta_period</code>	Absolute value of the difference between the <code>Multiband_period</code> and the MHAOV period obtained using a single band	This work
<code>IAR_phi</code> *	Level of autocorrelation using a discrete-time representation of a DRW model	Eyheramendy et al. (2018)
MHPS parameters*	Obtained from a MHPS analysis (three in total)	Arévalo et al. (2012)
<code>positive_fraction</code>	Fraction of detections in the difference-images of a given band which are brighter than the template image	This work
<code>Power_rate</code> * $\blacklozenge$	Ratio between the power of the multiband periodogram obtained for the best period candidate ( $P$ ) and $2 \times P$ , $3 \times P$ , $4 \times P$ , $P/2$ , $P/3$ or $P/4$	This work
<code>PPE</code> * $\blacklozenge$	Multiband Periodogram Pseudo Entropy	This work
<code>(g-r)_max</code> $\blacklozenge$	$g-r$ color obtained using the brightest <code>lc_diff</code> magnitude in each band	This work
<code>(g-r)_max_corr</code> $\blacklozenge$	$g-r$ color obtained using the brightest <code>lc_corr</code> magnitude in each band	This work
<code>(g-r)_mean</code> $\blacklozenge$	$g-r$ color obtained using the mean <code>lc_diff</code> magnitude of each band	This work
<code>(g-r)_mean_corr</code> $\blacklozenge$	$g-r$ color obtained using the mean <code>lc_corr</code> magnitude of each band	This work
<code>delta_mag_fid</code>	Difference between maximum and minimum observed magnitude in a given band	This work
<code>ExcessVar</code> **	Measure of the intrinsic variability amplitude	Allevato et al. (2013)
<code>GP_DRW_tau</code> **	Relaxation time $\tau$ from DRW modeling	Graham et al. (2017)
<code>GP_DRW_sigma</code> **	Amplitude of the variability at short timescales ( $t \ll \tau$ ), from DRW modeling	Graham et al. (2017)
Harmonics parameters*	Obtained by fitting a harmonic series up to the seventh harmonic (14 in total)	(Stellingwerf & Donohoe 1986)
<code>Multiband_period</code> * $\blacklozenge$	Period obtained using the multiband MHAOV periodogram	Mondrik et al. (2015)
<code>Pvar</code> **	Probability that the source is intrinsically variable	McLaughlin et al. (1996)
<code>SF_ML_amplitude</code> **	rms magnitude difference of the SF, computed over a 1 yr timescale	Schmidt et al. (2010)
<code>SF_ML_gamma</code> **	Logarithmic gradient of the mean change in magnitude	Schmidt et al. (2010)
SPM features*	Supernova parametric model features (seven in total)	Villar et al. (2019b)
<code>Amplitude</code>	Half of the difference between the median of the maximum 5% and of the minimum 5% magnitudes	Richards et al. (2011)
<code>AndersonDarling</code>	Test of whether a sample of data comes from a population with a specific distribution	Nun et al. (2015)
<code>Autocor_length</code>	Lag value where the auto-correlation function becomes smaller than <code>Eta_e</code>	Kim et al. (2011)
<code>Beyond1Std</code>	Percentage of points with photometric mag that lie beyond $1\sigma$ from the mean	Richards et al. (2011)

Con	Number of three consecutive data points brighter/fainter than $2\sigma$ of the light curve	Kim et al. (2011)
Eta_e	Ratio of the mean of the squares of successive mag differences to the variance of the light curve	Kim et al. (2014)
Gskew	Median-based measure of the skew	Nun et al. (2015)
LinearTrend	Slope of a linear fit to the light curve	Richards et al. (2011)
MaxSlope	Maximum absolute magnitude slope between two consecutive observations	Richards et al. (2011)
Meanvariance	Ratio of the standard deviation to the mean magnitude	Nun et al. (2015)
MedianAbsDev	Median discrepancy of the data from the median data	Richards et al. (2011)
MedianBRP	Fraction of photometric points within amplitude/10 of the median mag	Richards et al. (2011)
PairSlopeTrend	Fraction of increasing first differences minus fraction of decreasing first differences over the last 30 time-sorted mag measures	Richards et al. (2011)
PercentAmplitude	Largest percentage difference between either max or min mag and median mag	Richards et al. (2011)
Psi_CS	Range of a cumulative sum applied to the phase-folded light curve	Kim et al. (2011)
Psi_eta	Eta_e index calculated from the folded light curve	Kim et al. (2014)
Q31	Difference between the 3 <sup>rd</sup> and the 1 <sup>st</sup> quartile of the light curve	Kim et al. (2014)
Rcs	Range of a cumulative sum	Kim et al. (2011)
Skew	Skewness measure	Richards et al. (2011)
SmallKurtosis	Small sample kurtosis of the magnitudes	Richards et al. (2011)
Std	Standard deviation of the light curve	Nun et al. (2015)
StetsonK	Robust kurtosis measure	Kim et al. (2011)

### 3.1.1. Further description of some relevant detection features

Table 2 summarizes the definitions of the detection features used by the light curve classifier. However, some of these features are worth describing in more detail, either because they are new features, or because the changes we made to them were sufficiently relevant that further explanation is in order (see also Appendix A):

- **Multiband Period:**

The period is estimated using the Multi Harmonic Analysis of Variance (MHAOV) periodogram (Schwarzenberg-Czerny 1996), which is based on fitting periodic orthogonal polynomials to the data. A single period estimate per light curve is computed by fitting both bands using the MHAOV multiband extension proposed by Mondrik et al. (2015). We denote this period as `Multiband_period`. For sources with detections only in  $g$  or only in  $r$ , the `Multiband_period` reports the single band period. To avoid overfitting the data when few samples are available we set the number of harmonics to one. This might not capture the best period for non-sinusoidal light curves, e.g., detached and semi-detached eclipsing binaries, returning a harmonic instead. We found that having a harmonic of the true period is

in general sufficient to classify non-sinusoidal light curves correctly given that other features such as the `power_rate` are included. We choose MHAOV for this analysis as it provides a good trade-off between performance and computational complexity.

- **Periodogram Pseudo Entropy:**

To have an estimate of the confidence of the candidate period (obtained with the multiband MHAOV method), we developed a heuristic based on the entropy of the normalized periodogram peaks, which we denote as periodogram pseudo entropy (PPE). This value is computed by recovering the 100 largest values of the periodogram, normalizing them so they add to 1 and computing the entropy of that vector. This feature is computed as

$$PPE = 1 + \frac{1}{\log(100)} \sum_{i=1}^{100} \left(\frac{p_i}{Z}\right) \log\left(\frac{p_i}{Z}\right), \quad (1)$$

where  $p_i$  is the value of the  $i$ -th largest peak of the periodogram and  $Z = \sum_{i=1}^{100} p_i$ . This feature takes values between zero (no clear period stands out) and one (periodogram has a single large peak).

- **Power Rate:** Ratio between the power of the multiband periodogram obtained for the best period candidate ( $P$ ) versus the power of the multiband periodogram obtained for  $n$  times this period [`Power_rate_n` =  $Power(P)/Power(n \times P)$ ], where  $n$  can take values of 2, 3, 4, 1/2, 1/3, and 1/4. We computed these ratios in order to detect cases where we measure an aliased multiple of the period instead of the true period, which is particularly a common issue for some classes of eclipsing binaries (e.g., [Catelan et al. 2013](#); [Graham et al. 2013](#); [McWhirter et al. 2018](#); [VanderPlas 2018](#), and references therein).
- **Harmonics parameters:** Harmonic series ([Stellingwerf & Donohoe 1986](#)) are commonly used to model and classify periodic light curves ([Debosscher et al. 2007](#); [Sarro et al. 2009](#); [Richards et al. 2011](#); [Elorrieta et al. 2016](#)). In this work we fit a harmonic series up to the seventh harmonic, according to the expression

$$y(t_j) = \sum_{k=1}^7 \left[ A_k \cos\left(\frac{2\pi k t_j}{P}\right) + B_k \sin\left(\frac{2\pi k t_j}{P}\right) \right] + C, \quad (2)$$

where  $t_j$  corresponds to the observational time of the  $j$ -th detection,  $P$  is the best candidate period computed from the multiband periodogram as above, and  $y(t_j)$  is the magnitude estimated by the harmonic model. Even though we use the `Multiband_period`, the harmonic model is computed using the detections in each band independently.  $A_k$ ,  $B_k$  and  $C$  for  $k = 1, \dots, 7$  are obtained by minimizing the weighted mean square error between the observed magnitudes and the model.

Note that the model is linear with respect to its parameters, so the latter can be computed using weighted linear regression. The inverse of the square of each observational error is used as a weight, which minimizes contributions from noisier observations. The cost function is given by

$$\min_{A_k, B_k} \frac{1}{J} \sum_{j=1}^J \frac{[\text{mag}(t_j) - y(t_j)]^2}{\text{sigma}(t_j)^2}, \quad (3)$$

where  $J$  is the number of observations,  $\text{mag}(t_j)$  is the observed magnitude at time  $t_j$ , and  $\text{sigma}(t_j)$  is the observational error at time  $t_j$ . The solution to the weighted least squares optimization problem is found using the Moore-Penrose pseudoinverse.

This solution has the additional property of having the minimum Euclidean norm when the problem is underdetermined ([Ben-Israel & Greville 2003](#)), which in this case corresponds to having less than 15 observations.

Once the parameters are learnt, equation 2 can be rewritten as

$$y(t_j) = \sum_{k=1}^7 M_k \cos\left(\frac{2\pi k t_j}{P} - \phi_k\right) + C, \quad (4)$$

with  $M_k = \sqrt{A_k^2 + B_k^2}$  and  $\phi_k = \arctan(B_k/A_k)$ . In this way, the harmonics are now described by the amplitude and phase of each component. The model is shifted in time in order to have zero phase in the first harmonic, which is done following the expression  $\phi'_k = \phi_k - k\phi_1$ , replacing  $\phi_k$  by  $\phi'_k$  in Eq. 4.

Finally, the parameters  $M_k$  for  $k = 1, \dots, 7$ ,  $\phi'_k$  for  $i = 2, \dots, 7$  and the mean square error are used as features, which are denoted `Harmonics_mag_1`, ..., `Harmonics_mag_7`, `Harmonics_phase_2`, ..., `Harmonics_phase_7`, `Harmonics_mse`, respectively.

- **Supernova parametric model (SPM):** [Villar et al. \(2019b\)](#) introduced an analytic model describing SN light curves as a six parameter function, which they used to characterize and classify SN light curves from the Pan-STARRS1 Medium-deep Survey ([Chambers et al. 2016](#)). This model is an extension of previous empirical efforts to analytically describe supernova light curves, including the effects of different explosion times, normalization factors, initial rise timescales, rate of decline after peak, plateau lengths, or tail decay timescales. We introduce two modifications to this model. First we reparametrize the function to always remain positive in a simple validity range, i.e., one defined by a set of inequalities involving at most one variable per inequality, changing the validity range accordingly. After the first modification, the model is the following:

$$F = \begin{cases} \frac{A \left(1 - \beta^t \frac{t-t_0}{t_1-t_0}\right)}{1 + \exp\left(-\frac{t-t_0}{\tau_{\text{rise}}}\right)} & \text{if } t < t_1 \\ \frac{A(1 - \beta^t) \exp\left(-\frac{t-t_1}{\tau_{\text{fall}}}\right)}{1 + \exp\left(-\frac{t-t_0}{\tau_{\text{rise}}}\right)} & \text{if } t \geq t_1, \end{cases} \quad (5)$$

where we also use  $\gamma \equiv t_1 - t_0$  as a parameter instead of  $t_1$ . This function is positive valued when  $A > 0$ ,  $\gamma > 0$ ,  $\tau_{\text{rise}} > 0$ ,  $\tau_{\text{fall}} > 0$  and  $0 < \beta' < 1$ .

The second difference with respect to Villar et al. (2019a) is replacing the piecewise-defined function for a soft transition between the two components. This is done by including a sigmoid function  $\sigma(t) = 1/(1 + \exp(-t))$ , which allows a soft transition between zero and one. As the parameter  $t_1$  defines the transition between the two pieces of the model in Eq. 5, it cannot be optimized properly using first-order methods. Our proposed model allows using this technique effectively to learn the parameters of the model, which is given by the following equation:

$$F = \frac{A \left(1 - \beta' \frac{t-t_0}{t_1-t_0}\right)}{1 + \exp\left(-\frac{t-t_0}{\tau_{\text{rise}}}\right)} \cdot \left[1 - \sigma\left(\frac{t-t_1}{3}\right)\right] + \frac{A(1 - \beta') \exp\left(-\frac{t-t_1}{\tau_{\text{fall}}}\right)}{1 + \exp\left(-\frac{t-t_0}{\tau_{\text{rise}}}\right)} \cdot \left[\sigma\left(\frac{t-t_1}{3}\right)\right]. \quad (6)$$

In this particular model, for all the sources we use the light curves based on the difference images (`lc.diff`). This is done to avoid the contamination from unrelated host galaxy emission, which can distort the real shape of the SNe light curves. We also subtract from  $t$  the MJD value of the first detection observed for a given source. We computed  $A$  (`SPM_A`),  $\beta'$  (`SPM_beta`),  $t_0$  (`SPM_t0`),  $\gamma$  (`SPM_gamma`),  $\tau_{\text{rise}}$  (`SPM_tau_rise`), and  $\tau_{\text{fall}}$  (`SPM_tau_fall`), for each band independently. In addition, we computed the reduced  $\chi^2$  of the fit for the light curve, denoted as `SPM_chi`. The parameters are found using the function `curve_fit` provided by the Scipy library (Virtanen et al. 2020).

- Irregular autoregressive (IAR) model: Eyheramendy et al. (2018) introduced this model. It is a discrete-time representation of the continuous autoregressive model of order 1 [CAR(1) or DRW], which has desirable statistical properties such as strict stationarity and ergodicity without a distributional assumption. The IAR model is defined by

$$y_{t_j} = \phi^{t_j - t_{j-1}} y_{t_{j-1}} + \sigma \sqrt{1 - \phi^{2(t_j - t_{j-1})}} \varepsilon_{t_j}, \quad (7)$$

where  $\varepsilon_{t_j}$  is a white noise sequence with zero mean and unit variance,  $\sigma$  is the standard deviation of  $y_{t_j}$ , and  $\{t_j\}$  are the observational times for  $j = 1, \dots, n$ . We used a modified version of the IAR model, which considers the estimated variance of the measurement errors  $\delta_{t_j}^2$  in the likelihood of the model. Thus, by assuming a Gaussian distribution, the negative log-likelihood of the process is given by

$$\ell(\theta) = \frac{n}{2} \log(2\pi) + \frac{1}{2} \sum_{j=1}^n \log \nu_{t_j} + \frac{1}{2} \sum_{j=1}^n \frac{e_{t_j}^2}{\nu_{t_j}}, \quad (8)$$

where  $e_{t_1} = y_{t_1}$ ,  $\nu_{t_1} = \sigma^2 + \delta_{t_1}^2$ , and  $\hat{y}_{t_1} = 0$  are the initial values, while  $\hat{y}_{t_j} = \phi^{t_j - t_{j-1}} y_{t_{j-1}}$ ,  $e_{t_j} = y_{t_j} - \hat{y}_{t_j}$ , and  $\nu_{t_j} = \sigma^2(1 - \phi^{2(t_j - t_{j-1})}) + \delta_{t_j}^2$  for  $j = 2, \dots, n$ . Particularly,  $\phi$  describes the autocorrelation function of order 1 for a given light curve. We computed the maximum likelihood estimation of the parameter  $\phi$  (obtained directly from the light curves), and we used this as a feature for our classifier. We denoted this parameter as `IAR_phi`.

- Mexican Hat Power Spectrum (MHPS): Arévalo et al. (2012) proposed a method to compute low-resolution power spectra from data with gaps, where the light curves are convolved with a Mexican hat filter:  $F(x) \propto \left[1 - \frac{x^2}{\sigma^2}\right] e^{-x^2/2\sigma^2}$ . Gaps, or generally uneven sampling, are corrected for by convolving a unit-valued mask with the same sampling as the light curve and dividing the convolved light curve by it. This method can be used to isolate structures with a characteristic timescale ( $t \sim \sigma/\sqrt{2\pi^2}$ ) in a given light curve, in order to estimate the light curve variance associated with that timescale. We compute the light curve variance at two different timescales of 10 and 100 days. The variance associated with the 10 day timescale (“high” frequency) is denoted `MHPS_high`, while the variance associated with the 100 day timescale (“low” frequency) is denoted `MHPS_low`. We also compute the ratio between the low and high frequency variances for a given band, denoted as `MHPS_ratio`. The logarithm of `MHPS_ratio` is therefore an estimate of the power law slope of the power spectrum of the light curve.

### 3.2. Non-detection Features

For each detection, the ZTF alert stream includes  $5\text{-}\sigma$  magnitude limits (`diffmaglim`), which are computed

from the  $g$  and  $r$  difference images of the same area of the sky obtained in the previous 30 days, where the target associated with the alert was not detected (non-detections). These non-detections are very informative, since they can, for instance, inform us whether a transient has not been detected before; whether a non-variable source has begun to exhibit a variable behavior; or which range of observed magnitudes we should expect to measure when there are not significant differences between the science and template images, and an alert is not generated. The light curve classifier uses nine different features defined using all the non-detections associated with a given source, computed for both  $g$  and  $r$  bands, yielding a total of 18 non-detection features. Note that all these features are new, and have not been used before for classification. Table 3 lists the non-detection features used by the light curve classifier. As before, non-detection features ending with “\_1” are computed for the  $g$  band, and features ending with “\_2” are computed for the  $r$  band.

#### 4. CLASSIFICATION ALGORITHMS

The labeled set used in this work presents a very high imbalance (see Table 1). For instance, QSOs represent 75.4% of the stochastic sources, while CV/Novae represent just 2.5%. To deal with this issue, we looked for ML algorithms available in the literature that are designed to mitigate the imbalance problem. In particular, we worked with the `imbalanced-learn` Python package (Lemaître et al. 2017). `Imbalanced-learn` includes implementations of several re-sampling algorithms that are commonly used to handle data sets with strong between-class imbalance. The algorithms available in this package are fully compatible with `scikit-learn` methods.

In the following sections we describe the Random Forest (RF) algorithm used by the light curve classifier, as well as other tested ML algorithms. To train each classifier we randomly split the labeled set into a training set (80%) and testing set (20%) in a stratified fashion, preserving the percentage of samples for each class.

##### 4.1. *Balanced Hierarchical Random Forest*

A Decision Tree (Rokach & Maimon 2008) is a predictive algorithm that uses a tree structure to perform successive partitions on the data according to a certain criterion (e.g., a cut-off value in one of the descriptors or features) and produces possible decision paths, providing a final outcome for each path (the leaves of the tree). Decision Trees are commonly used for classification, where each final leaf is associated with a given class. RFs (Breiman 2001) are algorithms that build multiple Decision Trees, where each tree is trained us-

ing a random sub-sample of elements from a given training set, selected allowing repetition (bootstrap sample of the training set), and using a random selection of features. The final classification is obtained by averaging the classifications provided by each single tree. This average score can be interpreted as the probability ( $\mathcal{P}_{\text{RF}}$ ) that the input element belongs to a given class. One of the main advantages of RF is that it naturally provides a ranking of features for the classification, by counting the number of times each feature is selected to split the data.

Chen et al. (2004) proposed a modified RF that can deal with the imbalanced data classification. In their model each individual tree is trained using a sub-sample of the training set that is defined by generating a bootstrap sample from the minority class, and then randomly selecting the same number of cases, with replacement, from the majority classes. `Imbalanced-learn` implements the balanced RF classifier proposed by Chen et al. (2004). For the ALerCE light curve classifier we use their `BalancedRandomForestClassifier` method, selecting the hyper-parameters (number of trees, maximum number of features per tree, and maximum depth of each tree) with a K-Fold Cross-Validation procedure available in `scikit-learn`, with  $k = 5$  folds and using the “macro-recall” as target score (see its definition in Section 5.1).

##### 4.1.1. *The hierarchical classifier approach*

Considering the hierarchical structure of the taxonomy (see Section 2.2), we decided to construct a balanced hierarchical RF (BHRF) classifier. There are various approaches to perform a hierarchical classification (e.g., Silla & Freitas 2011; Naik & Rangwala 2018). In the particular case of the light curve classifier, we use a two-level scheme. The first level consists of a single classifier that separates the sources into three broad classes. The second level consists of three distinct classifiers, which further resolve each class in the first level into subclasses. We then use the probabilities obtained for each independent classifier to obtain the final classification.

In more detail, the first level (top level hereafter) consists of a single classifier which classifies every source as periodic, stochastic, or transient. The second level (bottom level hereafter) consists of three distinct classifiers: Transient, Stochastic, and Periodic. The classes considered by each of these three classifiers are the ones shown in Table 1 and Figure 3. Each classifier in the bottom level is trained using a training subset having only those classes included in the primary top class (for instance, the Transient classifier only includes sources

**Table 3.** List of non-detection features used by the light curve classifier. Note that “x” stands for either  $g$  or  $r$  bands.

Feature	Description
<code>dmag_first_det_fid</code>	Difference between the last non-detection <code>diffmaglim</code> in band “x” before the first detection in any band and the first detected magnitude in band “x”
<code>dmag_non_det_fid</code>	Difference between the median non-detection <code>diffmaglim</code> in the “x” band before the first detection and in any band the minimum detected magnitude (peak) in the “x” band
<code>last_diffmaglim_before_fid</code>	Last non-detection <code>diffmaglim</code> in the “x” band before the first detection in any band
<code>max_diffmaglim_before_fid</code>	Maximum non-detection <code>diffmaglim</code> in the “x” band before the first detection in any band
<code>max_diffmaglim_after_fid</code>	Maximum non-detection <code>diffmaglim</code> in the “x” band after the first detection in any band
<code>median_diffmaglim_before_fid</code>	Median non-detection <code>diffmaglim</code> in the “x” band before the first detection in any band
<code>median_diffmaglim_after_fid</code>	Median non-detection <code>diffmaglim</code> in the “x” band after the first detection in any band
<code>n_non_det_before_fid</code>	Number of non-detections in the “x” band before the first detection in any band
<code>n_non_det_after_fid</code>	Number of non-detections in the “x” band after the first detection in any band

classified as SNIa, SNIbc, SNII, and SLSN). It is important to note that these four classifiers are independent and process the same input features set described in Section 3. The final classification is constructed by multiplying the probabilities obtained for each class of the top level [ $\mathcal{P}_{top}(transient)$ ,  $\mathcal{P}_{top}(stochastic)$ , and  $\mathcal{P}_{top}(periodic)$ ] with the individual probabilities obtained by their correspondent classifier in the bottom level. Namely, the probabilities of the Transient classifier ( $\mathcal{P}_T$ ) are multiplied by  $\mathcal{P}_{top}(transient)$ , the probabilities of the Stochastic classifier ( $\mathcal{P}_S$ ) are multiplied by  $\mathcal{P}_{top}(stochastic)$ , and the probabilities of the Periodic classifier ( $\mathcal{P}_P$ ) are multiplied by  $\mathcal{P}_{top}(periodic)$ . We denote the product of these probabilities as  $\mathcal{P}$ . For instance, the probability of a given source being an RRL corresponds to the product of its probability of being periodic (according to the top level) and its probability of being an RRL (according to the Periodic classifier):

$$\mathcal{P}(RRL) = \mathcal{P}_{top}(periodic) \cdot \mathcal{P}_P(RRL),$$

while the probability of being a Blazar is computed as:

$$\mathcal{P}(Blazar) = \mathcal{P}_{top}(stochastic) \cdot \mathcal{P}_S(Blazar).$$

Following this, the sum of the probabilities of the 15 classes for a given source adds up to one. Finally, the class of a given object is determined by selecting the class with the maximum  $\mathcal{P}$ .

The best cross-validation performance was obtained with the following hyper-parameter setting: 500 trees in each classifier, maximum depth trees (the nodes are expanded until all leaves are pure), and a maximum number of features equal to the square root of the total number of features, except for the Stochastic classifier, where we used 20% of the features. In Section 5 we present the

results obtained when applying the BHRF classifier to the ZTF data.

#### 4.2. Additional ML algorithms tested

In addition to RF, we also tested two other supervised classification algorithms: Gradient Boosting and Multilayer Perceptron. These tests were done as a complementary analysis, with the purpose of guiding future efforts in improving the light curve classifier.

None of these methods has a Python implementation particularly designed to handle imbalanced data sets; however, using `imbalanced-learn` we can generate balanced training sets. We present the results obtained using both classifiers in Section 5.

##### 4.2.1. Gradient Boosting

Gradient Boosting (GBoost; Friedman 2001) is an ML algorithm that uses an ensemble of weak prediction models (e.g., Decision Trees) to produce a more robust classification. The method implements a boosting algorithm (using a Gradient Descent algorithm) that trains a sequence of weak models, each compensating the weaknesses of its predecessors. `eXtreme Gradient Boosting` (XGBoost; Chen & Guestrin 2016) is a package available in several computing languages (including Python) that implements GBoost algorithms for classification and regression in an efficient and scalable way. It has become one of the most used packages for regression and classification in recent years.

For the case of GBoost we followed the same two-level hierarchical strategy described in Section 4.1.1. However, since the current version of the XGBoost multi-class classifier was not designed to deal with highly imbalanced data sets (e.g., Wang et al. 2019), we tested a model that uses XGBoost

and is trained with a balanced training set. We constructed this balanced training set using the `RandomUnderSampler` and `RandomOverSampler` methods available in `imbalanced-learn`. For the case of the top level, Periodic, and Stochastic classifiers, we constructed a balanced training set by generating 10 random samples using the `RandomUnderSampler` method, resampling all classes (‘all’ sampling strategy), and concatenating them, in order to obtain a training set with more than 10,000 objects in total for each classifier. For the case of the Transient classifier we used the `RandomOverSampler` method, resampling all classes, to generate one random sample with  $\sim 600$  objects. Each classifier uses the default hyper-parameters defined by the `XGBoost` Python package, with the exception of the boosting rounds, where we used 500, and the objective function, which was set up to do multi-class classification, using the softmax function (‘multi:softmax’). As in the case of the BHRF model, the class of a given object is determined by selecting the class with the maximum probability (obtained by multiplying the probabilities of the top and bottom levels).

#### 4.2.2. Multilayer Perceptron

Artificial neural networks (ANNs) are mathematical models inspired by the human brain. ANNs are composed of elemental computational units called neurons (Haykin 1994). ANNs can be used to perform complex tasks such as classification or regression. A Multilayer Perceptron (MLP) corresponds to an ANN whose neurons are ordered by layers, where all neurons belonging to a given layer receive the same input vector and each unit processes this vector independently according to its own parameters. The outputs of all neurons in a layer are grouped and form the input vector for the next layer. For the case of classification, when using the softmax activation function, the final layer provides the probabilities that a given element belongs to a given class. One way of obtaining the final class is to assign the label with the maximum probability in the output layer.

For this model, we also followed the two-level hierarchical strategy described in Section 4.1.1. We tested different MLP architectures, changing the number of layers and the number of neurons per layer. We used the `Keras` API provided by the Python version of `TensorFlow 2.0` (Abadi et al. 2016). We split the original training set defined above into a new training set (80%) and a validation set (20%). In order to deal with the high imbalance of the training set we used the balanced mini-batches generator for `Keras` provided by the `imbalanced-learn` Python package. The best performance (considering

the categorical cross-entropy loss and accuracy curves for the training and validation sets) was obtained using MLPs with two hidden layers with 256 and 128 neurons for all the classifiers (top level, Transient, Stochastic, and Periodic). Regularization via the dropout method (Srivastava et al. 2014) is used to prevent overfitting. The dropout fraction is set at 0.50.

## 5. RESULTS

### 5.1. Results for the BHRF classifier

In order to test the performance of our BHRF classifier we generated 20 different training and testing sets using the `ShuffleSplit` iterator provided by `scikit-learn`, which uses random permutations to split the data, using each time 80% of the labeled set as training set and 20% as testing set, preserving the percentage of samples for each class in the original labeled set. Then, we trained 20 different BHRF models using each training set, and tested their performance using the corresponding testing sets. We emphasize that the testing sets are never used in training their respective models.

Table 4 lists three different scores: precision, recall, and F1-score. Despite the high imbalance present in the labeled set, all classes are equally important, thus we computed macro-averaged scores:

$$\text{Precision} = \frac{1}{n_{cl}} \sum_{i=1}^{n_{cl}} \frac{TP_i}{TP_i + FP_i}, \quad (9)$$

$$\text{Recall} = \frac{1}{n_{cl}} \sum_{i=1}^{n_{cl}} \frac{TP_i}{TP_i + FN_i}, \quad (10)$$

$$\text{F1-score} = 2 \times \frac{\text{Precision} \times \text{Recall}}{\text{Precision} + \text{Recall}}, \quad (11)$$

where  $n_{cl}$  is the total number of classes,  $TP_i$  is the number of true positives,  $FP_i$  the number of false positives, and  $FN_i$  is the number of false negatives, for a given class  $i$ . For the particular case of the BHRF classifier, Table 4 reports the mean and the standard deviation of the macro-averaged scores obtained by the 20 models when applying them to their respective testing sets.

In addition, Figures 6 and 7 show the confusion matrices obtained for the top and bottom levels, respectively. To generate these confusion matrices we used the results obtained when applying each of the 20 BHRF models to their corresponding testing sets, providing for each level the median and 5 and 95 percentiles of the confusion matrices obtained by each of the 20 models.

The confusion matrix of the top level shows that the classifier can recover more than 97% of the true labels, and that the contamination between classes is below 3%. The scores obtained reflect the good performance of the top level classifier.

**Table 4.** Macro-averaged scores obtained for each classifier in the testing set.

Classifier	Precision	Recall	F1-score
BHRF - top	$0.96 \pm 0.01$	$0.99 \pm 0.01$	$0.97 \pm 0.01$
BHRF - bottom	$0.57 \pm 0.01$	$0.76 \pm 0.02$	$0.59 \pm 0.01$
GBoost - top	0.99	0.99	0.99
GBoost - bottom	0.72	0.72	0.71
MLP - top	0.94	0.99	0.96
MLP - bottom	0.54	0.69	0.58

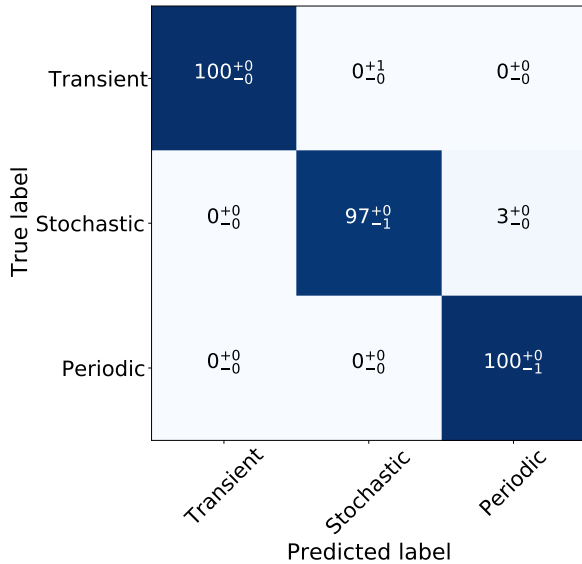


**Figure 6.** Confusion Matrix for the top level BHRF classifier. The confusion matrix was obtained by generating 20 different training and testing sets, and by training 20 independent models using each training set separately. After the training, each model is applied to their respective testing set. We provide the median and 5 and 95 percentiles of the confusion matrices obtained for the 20 testing sets. The reported values correspond to the percentages obtained by normalizing the matrices with the true labels. This level shows a high degree of accuracy with a low percentage of misclassifications.

For the case of the bottom level we obtained an F1-score of 0.59, implying significant confusion between classes. From Figure 7 we can see that the fraction of true positives in the confusion matrix of the bottom level has values between 50% and 100%, with mean, median and standard deviation of 78%, 76%, and 14%, respectively. In addition, from the figure it can be observed that the confusion is most often observed among classes with similar characteristics, like among the SN classes (particularly among SNIa versus SNIbc and SNII versus SLSN); among Blazar, AGN, and QSO classes; and among various periodic classes. The highest standard deviation of the predictions is observed for the case of

SLSN. This is a result of the low number of SLSN in the labeled set.

To complement our analysis, in Appendix B we provide the results obtained by a one-level multi-class RF model. From its results we can conclude that the light curve classifier improves considerably when a hierarchical strategy is followed.

#### 5.1.1. Comparison with the GBoost and MLP classifiers

In this work we tested two other classifiers: GBoost and MLP. For these models we present the results obtained by using 80% of the labeled set as a training set, and the remaining 20% as a testing set, preserving the percentage of samples for each class in the original labeled set. The scores obtained by these classifiers in the testing set are shown in Table 4. The confusion matrices obtained for the bottom level of the GBoost and MLP classifiers in the testing set are presented on the left and right sides of Figure 8, respectively.

The precision and F1-score obtained by GBoost are in general better than the ones obtained by the BHRF classifier, with the exception of the recall score of the bottom level. However, the fraction of true positives in the confusion matrix of the bottom level range between 5% and 100%, with a mean, median, and standard deviation of 72%, 83%, and 29%, respectively, which explain the lower recall obtained by GBoost, compared to the BHRF classifier. In addition, the classes with the largest fraction of true positives in the confusion matrix of GBoost correspond to the most populated classes in the labeled set, like QSOs, which represent 75.4% of the stochastic sources; SNIa, which represent 74.0% of the transients; or LPV, E, and RRL, which represent 16.2%, 43.5%, and 37.3% of the periodic sources, respectively. This is not observed in the results obtained by BHRF, where there is no evidence of correlation between the representativity of a given class and its fraction of true positives in the confusion matrix shown in Figure 7.

The results obtained using GBoost are promising. We obtained good scores although the current versions of GBoost available in the literature have not been designed to deal with high imbalance for the case of multi-

True label	SN Ia	$76^{+7}_{-6}$	$18^{+5}_{-6}$	$5^{+2}_{-2}$	$1^{+2}_{-1}$	$0^{+0}_{-0}$	$0^{+0}_{-0}$	$0^{+0}_{-0}$	$0^{+0}_{-0}$	$0^{+0}_{-0}$	$0^{+0}_{-0}$	$0^{+0}_{-0}$	$0^{+0}_{-0}$	$0^{+0}_{-0}$	$0^{+0}_{-0}$		
	SN Ibc	$33^{+11}_{-11}$	$50^{+17}_{-6}$	$11^{+11}_{-6}$	$6^{+11}_{-6}$	$0^{+0}_{-0}$	$0^{+0}_{-0}$	$0^{+0}_{-0}$	$0^{+0}_{-0}$	$0^{+0}_{-0}$	$0^{+0}_{-0}$	$0^{+0}_{-0}$	$0^{+0}_{-0}$	$0^{+0}_{-0}$	$0^{+6}_{-0}$		
	SN II	$15^{+8}_{-4}$	$16^{+10}_{-5}$	$53^{+7}_{-9}$	$17^{+9}_{-6}$	$0^{+0}_{-0}$	$0^{+2}_{-0}$	$0^{+0}_{-0}$	$0^{+0}_{-0}$	$0^{+2}_{-0}$	$0^{+0}_{-0}$	$0^{+0}_{-0}$	$0^{+0}_{-0}$	$0^{+0}_{-0}$	$0^{+0}_{-0}$	$0^{+0}_{-0}$	
	SLSN	$0^{+28}_{-0}$	$0^{+1}_{-0}$	$0^{+25}_{-0}$	$100^{+0}_{-26}$	$0^{+0}_{-0}$	$0^{+1}_{-0}$	$0^{+25}_{-0}$	$0^{+0}_{-0}$	$0^{+0}_{-0}$	$0^{+0}_{-0}$	$0^{+0}_{-0}$	$0^{+0}_{-0}$	$0^{+0}_{-0}$	$0^{+0}_{-0}$	$0^{+0}_{-0}$	
	QSO	$0^{+0}_{-0}$	$0^{+0}_{-0}$	$0^{+0}_{-0}$	$0^{+0}_{-0}$	$87^{+1}_{-1}$	$8^{+0}_{-0}$	$5^{+0}_{-1}$	$0^{+0}_{-0}$	$0^{+0}_{-0}$	$0^{+0}_{-0}$	$0^{+0}_{-0}$	$0^{+0}_{-0}$	$0^{+0}_{-0}$	$0^{+0}_{-0}$	$0^{+0}_{-0}$	
	AGN	$0^{+0}_{-0}$	$0^{+0}_{-0}$	$0^{+0}_{-0}$	$0^{+0}_{-0}$	$9^{+2}_{-1}$	$85^{+2}_{-2}$	$5^{+2}_{-1}$	$0^{+1}_{-0}$	$0^{+0}_{-0}$	$0^{+0}_{-0}$	$0^{+0}_{-0}$	$0^{+0}_{-0}$	$0^{+0}_{-0}$	$0^{+0}_{-0}$	$0^{+0}_{-0}$	
	Blazar	$0^{+0}_{-0}$	$0^{+0}_{-0}$	$0^{+0}_{-0}$	$0^{+0}_{-0}$	$17^{+2}_{-4}$	$7^{+1}_{-2}$	$74^{+5}_{-3}$	$1^{+1}_{-1}$	$1^{+2}_{-1}$	$0^{+1}_{-0}$	$0^{+0}_{-0}$	$0^{+0}_{-0}$	$0^{+0}_{-0}$	$0^{+0}_{-0}$	$0^{+1}_{-0}$	
	YSO	$0^{+0}_{-0}$	$0^{+0}_{-0}$	$0^{+0}_{-0}$	$0^{+0}_{-0}$	$0^{+0}_{-0}$	$0^{+1}_{-0}$	$1^{+0}_{-1}$	$78^{+3}_{-3}$	$0^{+1}_{-0}$	$4^{+1}_{-1}$	$1^{+1}_{-0}$	$0^{+1}_{-0}$	$1^{+2}_{-0}$	$3^{+1}_{-1}$	$11^{+2}_{-1}$	
	CV/Nova	$4^{+5}_{-3}$	$2^{+3}_{-1}$	$1^{+1}_{-0}$	$0^{+0}_{-0}$	$0^{+1}_{-0}$	$0^{+0}_{-0}$	$1^{+1}_{-1}$	$1^{+2}_{-1}$	$68^{+5}_{-5}$	$1^{+1}_{-1}$	$3^{+2}_{-1}$	$4^{+2}_{-2}$	$10^{+3}_{-3}$	$2^{+2}_{-1}$	$2^{+2}_{-1}$	
	LPV	$0^{+0}_{-0}$	$0^{+0}_{-0}$	$0^{+0}_{-0}$	$0^{+0}_{-0}$	$0^{+0}_{-0}$	$0^{+0}_{-0}$	$0^{+0}_{-0}$	$1^{+0}_{-0}$	$0^{+0}_{-0}$	$98^{+0}_{-1}$	$0^{+0}_{-0}$	$0^{+0}_{-0}$	$0^{+0}_{-0}$	$1^{+0}_{-1}$	$1^{+0}_{-1}$	
	E	$0^{+0}_{-0}$	$0^{+0}_{-0}$	$0^{+0}_{-0}$	$0^{+0}_{-0}$	$0^{+0}_{-0}$	$0^{+0}_{-0}$	$0^{+0}_{-0}$	$0^{+0}_{-0}$	$1^{+0}_{-0}$	$0^{+0}_{-0}$	$74^{+0}_{-2}$	$7^{+0}_{-1}$	$3^{+0}_{-0}$	$4^{+0}_{-1}$	$12^{+1}_{-1}$	
	DSCT	$0^{+0}_{-0}$	$0^{+0}_{-0}$	$0^{+0}_{-0}$	$0^{+0}_{-0}$	$0^{+0}_{-0}$	$0^{+0}_{-0}$	$0^{+0}_{-0}$	$0^{+0}_{-0}$	$0^{+0}_{-0}$	$0^{+0}_{-0}$	$5^{+3}_{-2}$	$89^{+3}_{-6}$	$2^{+3}_{-1}$	$1^{+1}_{-1}$	$3^{+2}_{-1}$	
	RRL	$0^{+0}_{-0}$	$0^{+0}_{-0}$	$0^{+0}_{-0}$	$0^{+0}_{-0}$	$0^{+0}_{-0}$	$0^{+0}_{-0}$	$0^{+0}_{-0}$	$0^{+0}_{-0}$	$0^{+1}_{-0}$	$0^{+0}_{-0}$	$4^{+1}_{-0}$	$4^{+0}_{-1}$	$87^{+0}_{-1}$	$2^{+0}_{-0}$	$2^{+1}_{-0}$	
	CEP	$0^{+0}_{-0}$	$0^{+1}_{-0}$	$0^{+0}_{-0}$	$0^{+0}_{-0}$	$0^{+0}_{-0}$	$0^{+0}_{-0}$	$0^{+1}_{-0}$	$1^{+1}_{-1}$	$0^{+1}_{-0}$	$0^{+2}_{-0}$	$3^{+2}_{-1}$	$1^{+2}_{-1}$	$11^{+5}_{-5}$	$76^{+4}_{-5}$	$9^{+3}_{-3}$	
	Periodic-Other	$0^{+0}_{-0}$	$0^{+0}_{-0}$	$0^{+0}_{-0}$	$0^{+0}_{-0}$	$0^{+0}_{-0}$	$0^{+0}_{-0}$	$0^{+0}_{-0}$	$1^{+1}_{-1}$	$1^{+1}_{-1}$	$2^{+0}_{-1}$	$11^{+2}_{-3}$	$3^{+1}_{-1}$	$5^{+2}_{-2}$	$5^{+2}_{-2}$	$73^{+4}_{-2}$	
			SN Ia	SN Ibc	SN II	SLSN	QSO	AGN	Blazar	YSO	CV/Nova	LPV	E	DSCT	RRL	CEP	Periodic-Other
		Predicted label															

**Figure 7.** As in Figure 6, but for the bottom level of the BHRF classifier. The black squares highlight the three classes of the top level (from top to bottom, transient, stochastic, and periodic, respectively). This matrix is quite diagonal, but shows more misclassification among related subtypes compared to the matrix obtained for the top level.

class classification. Therefore, further efforts should be done to implement GBoost in future versions of the light curve classifier. In particular, new implementations of GBoost for multi-class classification that follow similar approaches to the ones proposed by [Chen et al. \(2004\)](#) or [Wang et al. \(2019\)](#) should be tested, as should combinations of GBoost with data augmentation techniques (i.e., generating synthetic light curves of less populated classes using physical and/or statistical models).

For the case of the MLP classifier the scores obtained are in general lower compared to BHRF and GBoost. Its confusion matrix for the bottom level (see Figure 8) presents the same issues already discussed for the case of GBoost. The fraction of true positives in the confusion matrix ranges between 11% and 98%, with a mean, median, and standard deviation of 69%, 74%, and 22%, respectively. Therefore, we conclude that more

work should be done in order to obtain better results with MLP.

From these tests we can conclude that the BHRF is the model that currently achieves results that are less biased towards the most populated classes in the labeled set, i.e., it is able to predict all sub-classes, and the fraction of true positives does not correlate with how representative a given class in the labeled set is, compared to GBoost and MLP. Thus, we decided to use BHRF as the final model for the first version of the ALERCE light curve classifier. For the rest of this paper, presented results correspond to the BHRF classifier.

### 5.1.2. Results for the BHRF classifier excluding AllWISE data

We tested a version of the BHRF classifier that excludes features computed using AllWISE data. The macro-averaged precision, recall, and F1-score of the top level are 0.93, 0.97, and 0.95, respectively. For the bottom level the macro-averaged precision, recall, and F1-score are, respectively, 0.53, 0.72, and 0.55. These scores are slightly smaller than the ones obtained using the original version of the BHRF classifier. As can be observed in the confusion matrix shown in Figure 9, the stochastic classes are the most affected by the lack of AllWISE data, particularly YSOs and Blazars, whose fraction of true positives decreased 10% and 16%, respectively. This happens because of the similarities observed between the light curves of these and other classes, which are not easily separated using variability features alone. However, the results obtained by this version of the classifier are still good enough to be used in the case that AllWISE data are not available, as occurs, for instance, for faint objects.

### 5.2. Performance of the BHRF classifier as a function of magnitude and number of detections

As can be seen in Figure 5 for some classes, like YSOs, CEPs, and LPVs, a non-negligible fraction of sources in the labeled set have photometry available only in one band. It is therefore important to know how well the classifier behaves when a single band is available for a given source.

To evaluate this, we created 20 new testing sets defined considering only those sources with  $\geq 6$  detections in each band, from the 20 testing sets previously generated using the `ShuffleSplit` iterator (see Section 5.1). We then classified each new testing set with its respective model, considering: a) the features available for the  $g$  and  $r$  bands, b) the features available only for the  $g$  band, and c) the features available only for the  $r$  band. Figures 10 and 11 illustrate the results of this analysis. Figure 10 shows the recall as a function of the av-

erage magnitude for each subclass, with the exception of the SN classes which are grouped in one class called SN, while Figure 11 shows the recall as a function of the number of detections. From both figures we can infer that in general the best results are obtained when photometry from both  $g$  and  $r$  are available, with the exceptions of QSO, CEP and Periodic-Other classes.

From Figure 10 we can also conclude that the reliability of the classification versus the average magnitude is different for each class. These distributions in general follow the magnitude distribution in the labeled set of each class considered in this model (with the exception of RRL). For instance, for the labeled set, the CEP class corresponds to one of the brightest classes, having in general  $r < 16$ , while the LPV class covers a broader range of magnitudes. On the other hand, from Figure 11, we can infer that in general the classification improves when more detections are available in both bands, with the exceptions of the QSO and Periodic-Other classes.

The results obtained for Periodic-Other are not surprising since this class includes all the periodic classes not considered in the classifier (including several different types of pulsating stars, as well as the rotational variables). The results observed for the CEP class are probably due to the large fraction of CEPs in the labeled set with photometry only in the  $g$  band, which is produced by the saturation limit of the ZTF survey (12.5 to 13.2 magnitudes), and the fact that CEPs tend to be very bright particularly in the  $r$  band, and thus for bright CEPs the  $r$  band light curve is not available. For SNe, there is a decrease in the recall curve in the  $g$  band, presumably due to the fact that in general the  $g$ -band light curves of SNe tend to decay faster than the  $r$ -band light curves, producing shorter (and thus fewer detections)  $g$ -band light curves. This trend can be seen in the SN shown in Figure 2, as well as more generally in the light curve statistics for SNe. The average number of detections of SNe light curves is 12 and 16 in the  $g$  and  $r$  bands, respectively, and the total time length of SNe light curves corresponds to 53 and 64 days in the  $g$  and  $r$  bands, respectively. The low recall obtained for bright RRL when only the  $g$  band is available may be produced by differences in the variability features measured for different RRL sub-types. This issue is further discussed in Appendix C. The results obtained for AGNs and QSOs are likely related with incorrect labels, which we discuss further in Appendix D.

### 5.3. The deployed BHRF classifier

In order to use the BHRF classifier to classify the ZTF alert stream we need to train a single BHRF model. We

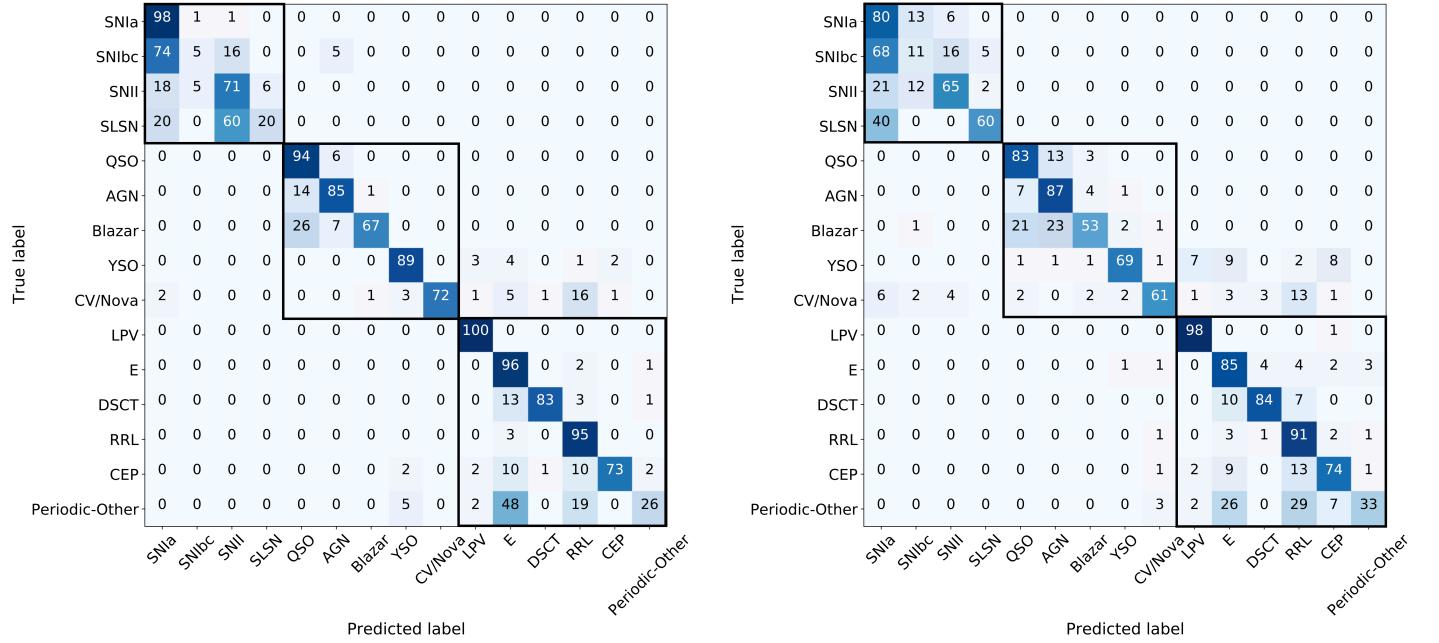


**Figure 8.** Confusion matrices of the bottom level obtained when applying the GBoost (left) and the MLP (right) classifiers to the testing set. The black squares highlight the three hierarchical classes (from top to bottom, transient, stochastic, and periodic, respectively). The reported values correspond to the percentages obtained by normalizing the matrix with the true labels. These matrices present a high percentage of misclassifications compared to the bottom level of the BHRF model (Figure 7).

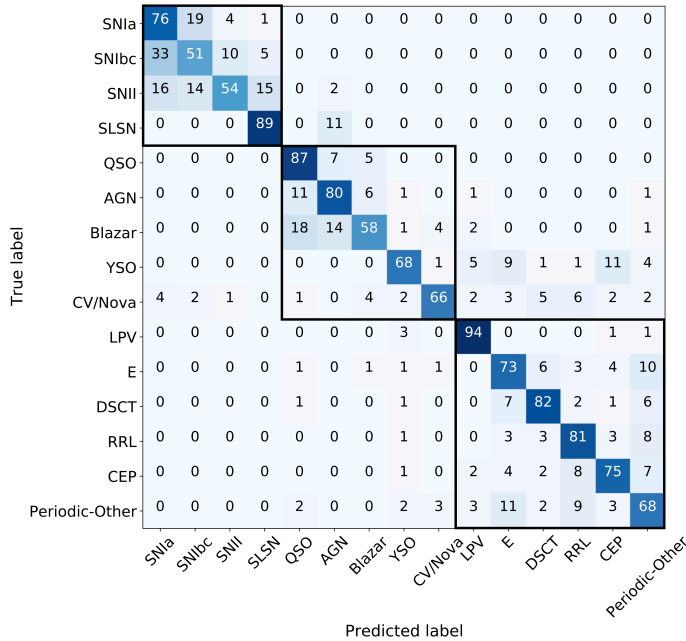


**Figure 9.** As in Figure 7, but for a model that excludes AllWISE data. We drop the errors, which are comparable to those listed in Figure 7, for simplicity. The results obtained for this model are reasonable, although the classification of some stochastic classes are affected by the lack of AllWISE data.

call this model “the deployed BHRF classifier”. As in the previous sections, we trained the deployed BHRF model using 80% of the labeled set as the training set and the remaining 20% as the testing set. Table 5 shows the classification report obtained for the bottom level of this classifier. From the table we can notice that in general the precision scores are lower than the recall scores. The results obtained for SNIa, SNII, QSO, AGN, YSO, CV/Nova, LPV, E, and RRL are good, with F1-score values higher than or equal to 0.60. This table also shows that some classes, such as the SNIbc, Periodic-Other, DSCT, and CEP classes, require further work in order to improve the results obtained by the classifier; this may involve data augmentation procedures, and better period estimations, as discussed in the following sections.

### 5.3.1. Feature ranking of the deployed BHRF classifier

In Table 6 we list the feature ranking (top 30) for each classifier within the two-level BHRF classifier (top level, Transient, Stochastic, and Periodic). The feature ranking is computed considering which features separate better the subclasses within each classifier, with more informative features having higher ranks (for more details see Hastie et al. 2009). From the table we can see that for all the classifiers, a considerable fraction of the top 30 features correspond to colors computed using the

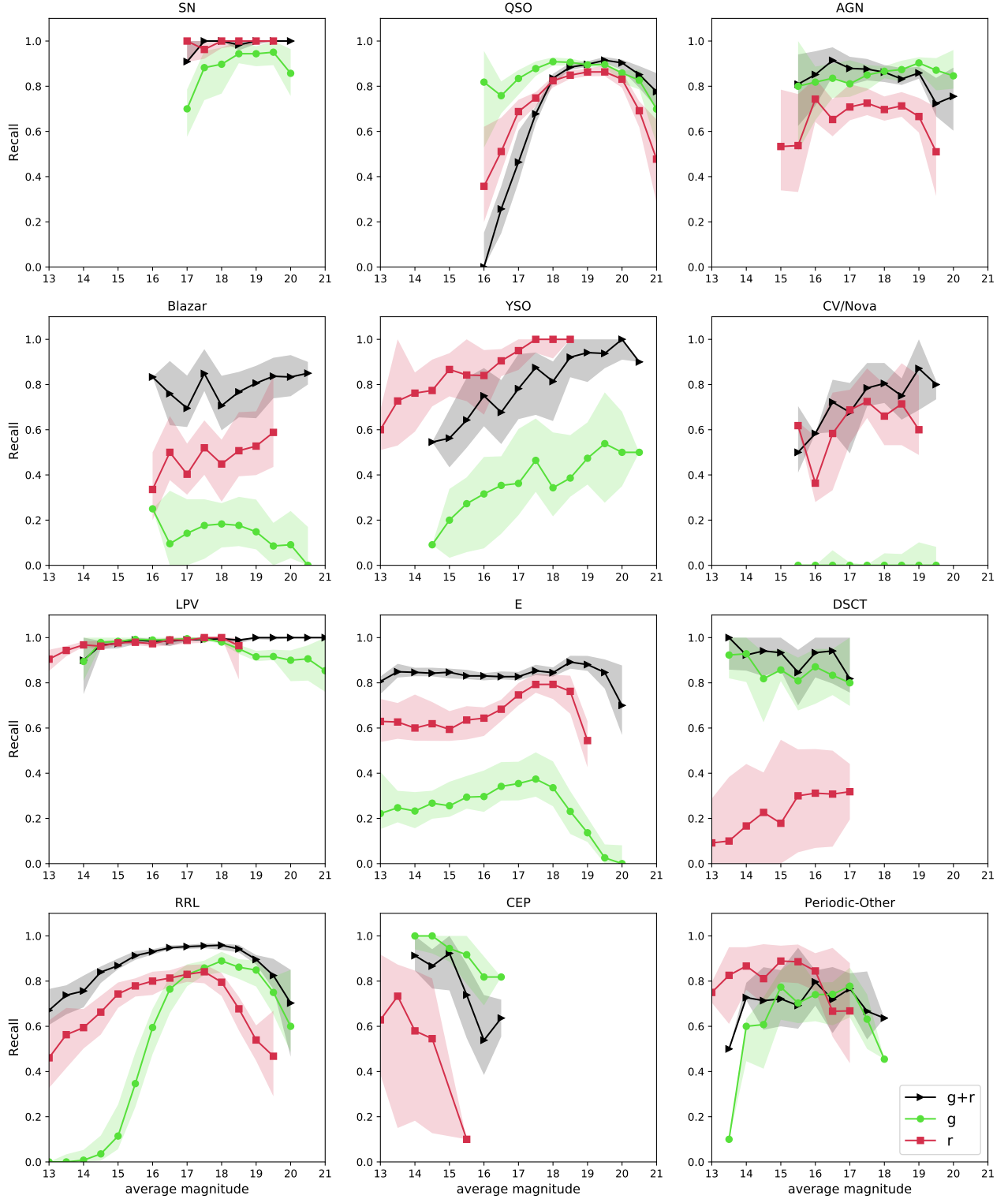


**Figure 10.** Recall for each stochastic and periodic subclass, as well as all transients (grouped as SN), as a function of the average magnitude. The x-axis ranges from 13 to 21 magnitudes, this range includes  $\sim 90\%$  of the sources. In black triangles we show the recall curves obtained when  $g$  and  $r$  photometries are available (considering the average magnitude in the  $g$  band), in green circles when only the  $g$  band is available, and in red squares when only the  $r$  band is available. The shaded regions were obtained by generating 20 different training and testing sets, and training 20 independent models using each of these sets. We report the median and 5 and 95 percentile values obtained from the 20 models. There is a truly wide variety of behaviors (see discussion in the text).

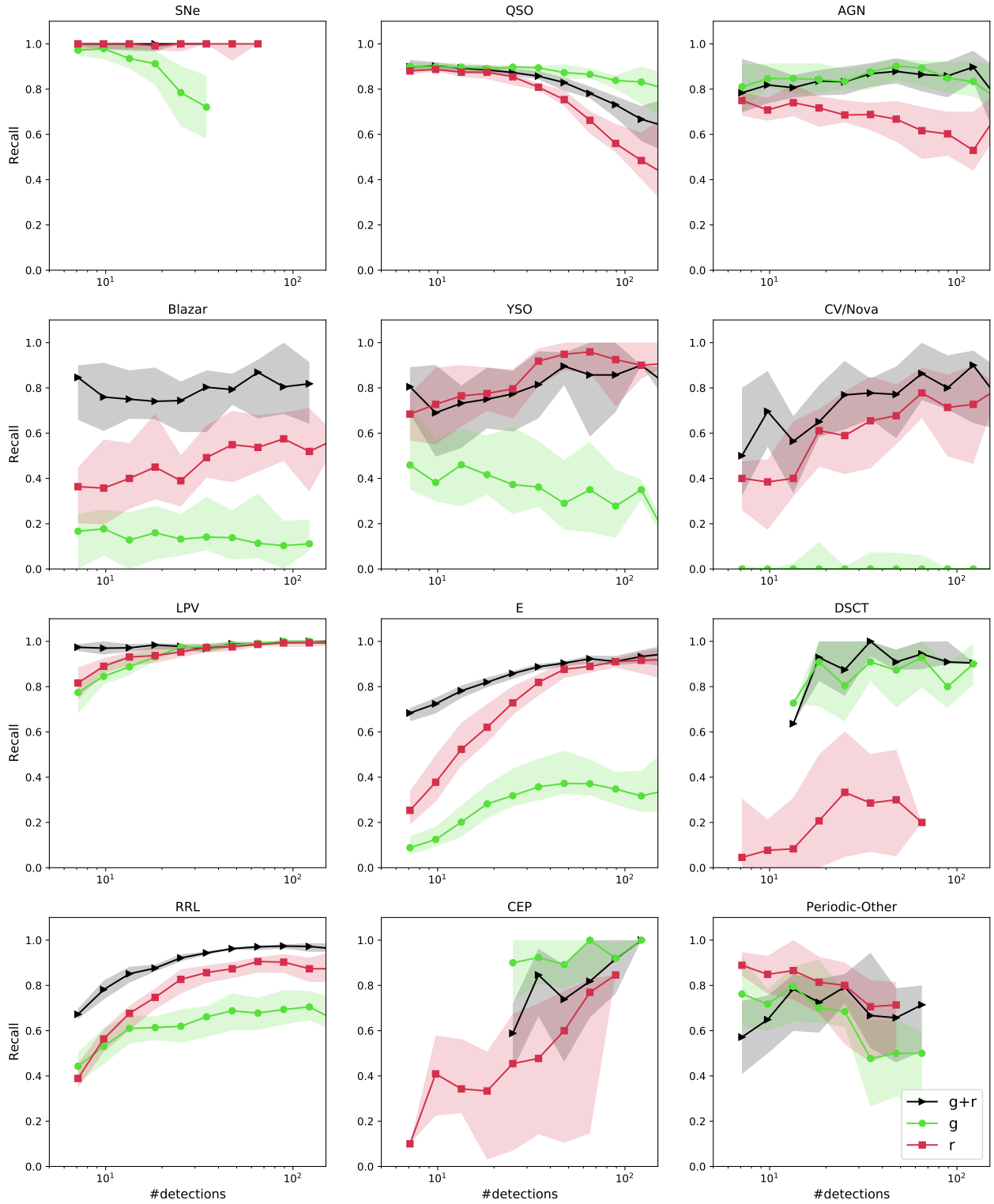


**Figure 11.** As in Figure 10, but plotting the Recall as a function of the number of detections in the light curve (in logarithmic scale). The x-axis ranges from 6 to 150 detections, this range includes  $\sim 90\%$  of the sources. Again, there is a wide variety of behaviors (see discussion in the text).

**Table 5.** Classification report of the bottom level of the deployed BHRF classifier. The last row shows the macro average of each score

Class	score	precision	recall	f1-score
SNIa	0.92	0.76	0.83	
SNIbc	0.14	0.58	0.23	
SNII	0.69	0.55	0.61	
SLSN	0.28	1.00	0.43	
QSO	0.97	0.87	0.92	
AGN	0.65	0.85	0.73	
Blazar	0.40	0.75	0.53	
YSO	0.73	0.78	0.75	
CV/Nova	0.52	0.71	0.60	
LPV	0.99	0.98	0.98	
E	0.95	0.74	0.83	
DSCT	0.15	0.89	0.26	
RRL	0.95	0.88	0.91	
CEP	0.18	0.75	0.29	
Periodic-Other	0.14	0.73	0.24	
macro avg	0.58	0.79	0.61	

ALLWISE and ZTF photometry, as well as new detection features (i.e., features not included in the FATS package) and non-detection features. Moreover, it can be observed that the ranking of features changes for each classifier.

The top level classifier is dominated by different types of features: ZTF and ALLWISE colors, morphological properties of the images (`sgscore1`), variability features related with the amplitude of the variability at short and long timescales (`MHPS_low`, `GP_DRW_sigma`, `Meanvariance`, `ExcessVar`, and `SPM_A`), variability features that detect smooth decrease or increase of the luminosity (`LinearTrend`, `SPM_tau_rise`, `SPM_tau_fall`), features related with the quality of a supernova parametric model fitting (`SPM_chi`), and features related with transient appearance or disappearance (`positive_fraction`, and `n_non_det_after_fid`).

On the other hand, the Transient classifier is dominated by the SPM features (e.g., `SPM_beta`, `SPM_t0`, `SPM_tau_rise`, and `SPM_tau_fall`). Other relevant features are the optical colors in the peak and the mean of the light curve, measured from the difference image light curves, features that detect smooth increase or decrease of the observed flux (`LinearTrend`), features that measure the level of correlation in the light curve (`IAR_phi`), features related with the amplitude of the variability (`MHPS_low`), and features related with the appearance of a transient source (`dmag_first_det_fid`, `last_diffmaglim_before_fid_1`). Note that SN rise re-

lated features, such as `SPM_t0` and `SPM_rise`, are some of the most relevant features for the classification of transients, and are crucial for the early classification of SNe. Also, note that `SPM_t0` is not the explosion time, but some characteristic time where the SN has risen significantly.

For the Stochastic classifier, 12 of the top 30 features are related with color, morphology and distance to the Galactic plane, and the rest correspond to features related with the amplitude of the variability observed at different time scales (e.g., `ExcessVar`, `SPM_A`, `Meanvariance`, `GP_DRW_sigma`, and `Amplitude`), and features related with the time scale of the variability (`IAR_phi`, `GP_DRW_tau`).

Finally, the Periodic classifier is clearly dominated by the `Multiband_period` feature, but also by different colors, by features related with the amplitude of the variability (e.g., `delta_mag_fid`, `Amplitude`, `ExcessVar`, `Meanvariance`, and `GP_DRW_sigma`), and features related with the timescale of the variations (e.g., `GP_DRW_tau`, and `IAR_phi`).

### 5.3.2. Results for the unlabeled ZTF set

We now turn to discuss the results obtained when applying the final BHRF classifier to all the sources in ZTF with  $\geq 6$  detections in  $g$  or  $\geq 6$  detections in  $r$ . Considering the data obtained by ZTF until 2020/06/09, there are 868,371 sources that satisfy this condition, hereafter defined as the “unlabeled ZTF set”. We define the class of a given object in the unlabeled ZTF set by selecting the class with the maximum probability obtained by the deployed BHRF classifier. However, users of this classifier can use the obtained probabilities to make their own probability cuts and select samples for their science. The features, classifications and probabilities obtained for the unlabeled ZTF set with data until 2020/06/09 are provided in a catalog that can be downloaded at [http://ml.alerce.online/lc\\_pred](http://ml.alerce.online/lc_pred).

It is important to note that the classifications obtained by the light curve classifier are updated every day, as new alerts are received. Whenever a new alert is received for a given source, the ALERCE pipeline recomputes its variability features and provides an updated classification. These updated classifications can be found at the [ALERCE Explorer website](#), using the “light curve classifier” tab, and specifying the desired class. Considering the results shown in Figure 11, we expect that the quality of the classification for a given source will improve as more detections are added to the light curve. In addition, with new alerts, more objects will satisfy the condition of having  $\geq 6$  detections in  $g$  or  $\geq 6$  detections in  $r$ , and thus, the size of the unlabeled ZTF set

**Table 6.** Feature ranking (top 30) for each layer of the deployed BHRF classifier.

Top level		Transient		Stochastic		Periodic	
Feature	Rank	Feature	Rank	Feature	Rank	Feature	Rank
W1-W2	0.094	SPM_t0_1	0.033	W1-W2	0.109	Multiband_period	0.089
sgscore1	0.053	SPM_beta_2	0.029	sgscore1	0.058	g-W2	0.062
positive_fraction_2	0.050	SPM_tau_rise_2	0.028	r-W2	0.049	r-W2	0.034
positive_fraction_1	0.048	SPM_tau_rise_1	0.025	(g-r)_mean_corr	0.048	(g-r)_max_corr	0.030
SPM_tau_rise_1	0.035	(g-r)_max	0.023	g-W2	0.046	g-W3	0.028
LinearTrend_2	0.032	SPM_t0_2	0.022	gal_b	0.045	(g-r)_mean	0.027
SPM_chi_1	0.031	LinearTrend_2	0.019	g-W3	0.037	(g-r)_max	0.025
g-W2	0.031	AndersonDarling_2	0.018	(g-r)_max_corr	0.035	GP_DRW_tau_1	0.023
g-W3	0.031	SPM_beta_1	0.017	ExcessVar_2	0.033	(g-r)_mean_corr	0.022
n_non_det_after_fid_2	0.026	SPM_tau_fall_2	0.017	Meanvariance_2	0.026	IAR_phi_1	0.022
W2-W3	0.025	dmag_first_det_fid_1	0.015	(g-r)_mean	0.025	Amplitude_1	0.017
SPM_beta_1	0.024	MHPS_low_1	0.013	delta_mag_fid_2	0.024	ExcessVar_1	0.017
SPM_tau_rise_2	0.023	LinearTrend_1	0.013	r-W3	0.023	delta_mag_fid_1	0.016
SPM_A_2	0.023	(g-r)_mean	0.012	W2-W3	0.022	Meanvariance_1	0.016
SPM_chi_2	0.020	MHPS_ratio_1	0.011	Amplitude_2	0.022	r-W3	0.016
SPM_A_1	0.019	SPM_tau_fall_1	0.011	Std_2	0.015	Std_1	0.015
r-W2	0.018	SPM_gamma_2	0.011	(g-r)_max	0.015	GP_DRW_sigma_1	0.015
ExcessVar_1	0.017	MHPS_ratio_2	0.010	SPM_A_2	0.014	GP_DRW_tau_2	0.012
ExcessVar_2	0.016	Skew_2	0.009	PercentAmplitude_2	0.013	PercentAmplitude_1	0.012
r-W3	0.014	sgscore1	0.009	SPM_A_1	0.012	W1-W2	0.009
Rcs_2	0.013	SPM_gamma_1	0.009	ExcessVar_1	0.011	W2-W3	0.009
GP_DRW_sigma_2	0.013	Power_rate_2	0.009	IAR_phi_1	0.010	SF_ML_amplitude_1	0.009
SPM_tau_fall_1	0.013	IAR_phi_2	0.009	GP_DRW_sigma_2	0.009	SPM_A_1	0.009
Meanvariance_2	0.012	dmag_first_det_fid_2	0.009	delta_mag_fid_1	0.009	Gskew_1	0.009
LinearTrend_1	0.012	IAR_phi_1	0.009	Pvar_2	0.007	Q31_1	0.009
SPM_beta_2	0.010	last_diffmaglim_before_fid_1	0.009	IAR_phi_2	0.007	Autocor_length_1	0.009
Pvar_2	0.010	PPE	0.008	GP_DRW_tau_2	0.007	IAR_phi_2	0.008
MHPS_low_2	0.009	Harmonics_mag_6_1	0.008	GP_DRW_tau_1	0.007	SF_ML_gamma_1	0.008
SF_ML_amplitude_2	0.009	MHPS_low_2	0.008	MHPS_high_1	0.007	Amplitude_2	0.007
(g-r)_max_corr	0.009	Gskew_2	0.008	MHPS_low_1	0.006	delta_mag_fid_2	0.007

increases every day. Moreover, with new detections the size of the labeled set will increase, allowing the training of new BHRF models. Updates regarding any possible modification to the light curve classifier (e.g., labeled set and models) will be published on the [ALeRCE Science website](#).

Figure 12 shows the number of candidates per class obtained for the 868,371 sources with enough alerts until 2020/06/09. Compared to Figure 4, it can be noticed that there is no correlation between the number of sources per class for the unlabel set and the number of sources per class for the labeled set. The Periodic-Other, E, and LPV classes have the highest number of candidates, while the SN classes have the lowest. The distribution of candidates per class is consistent with the astrophysical number densities (i.e., we are likely not misclassifying large numbers of sources). For instance, Blazars are relativistically beamed (and thus seen to have farther distances), but only over very small viewing

angles, and hence are expected to be less common than QSOs and AGNs. In the case of SNe, not factoring in the amount of time a particular SN is above the magnitude limits of the search (the “control time”), we find ratios of SNe II/SNe Ia and SNe Ibc/SN Ia of 0.21 and 0.41, respectively. Computing these ratios using the number of such classes reported from ASAS-SN discoveries in [Holoien et al. \(2019\)](#) yields 0.36 and 0.09, respectively. The significant differences between the SNe Ibc/SN Ia ratios implies that we are strongly overestimating the numbers of SN Ibc; given the similarities between SN Ibc and SN Ia light curves, we are likely classifying a non-negligible fraction of SN Ia as SN Ibc. This highlights the importance of including distance estimations to improve the classification of transients. We are currently working to include distance-based features in future versions of the classifier.

To investigate the quality of the predictions, we plotted the probability distributions of the top and bottom

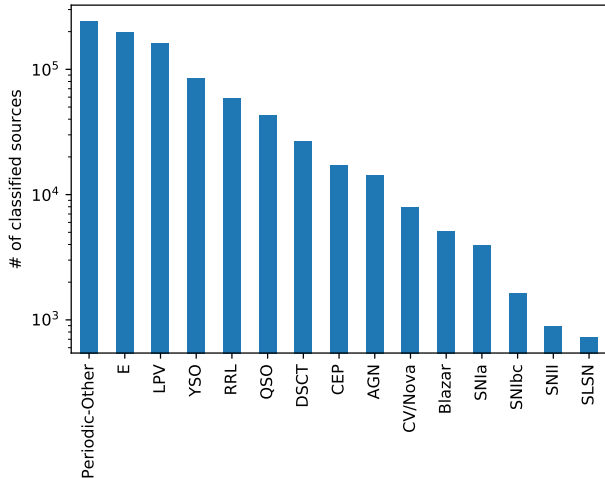


**Figure 12.** Number of candidates per class for all the sources in the unlabeled ZTF set. It can be seen that the number of sources per class for the unlabeled ZTF set does not correlate with the number of sources per class for the labeled set (see Figure 4).

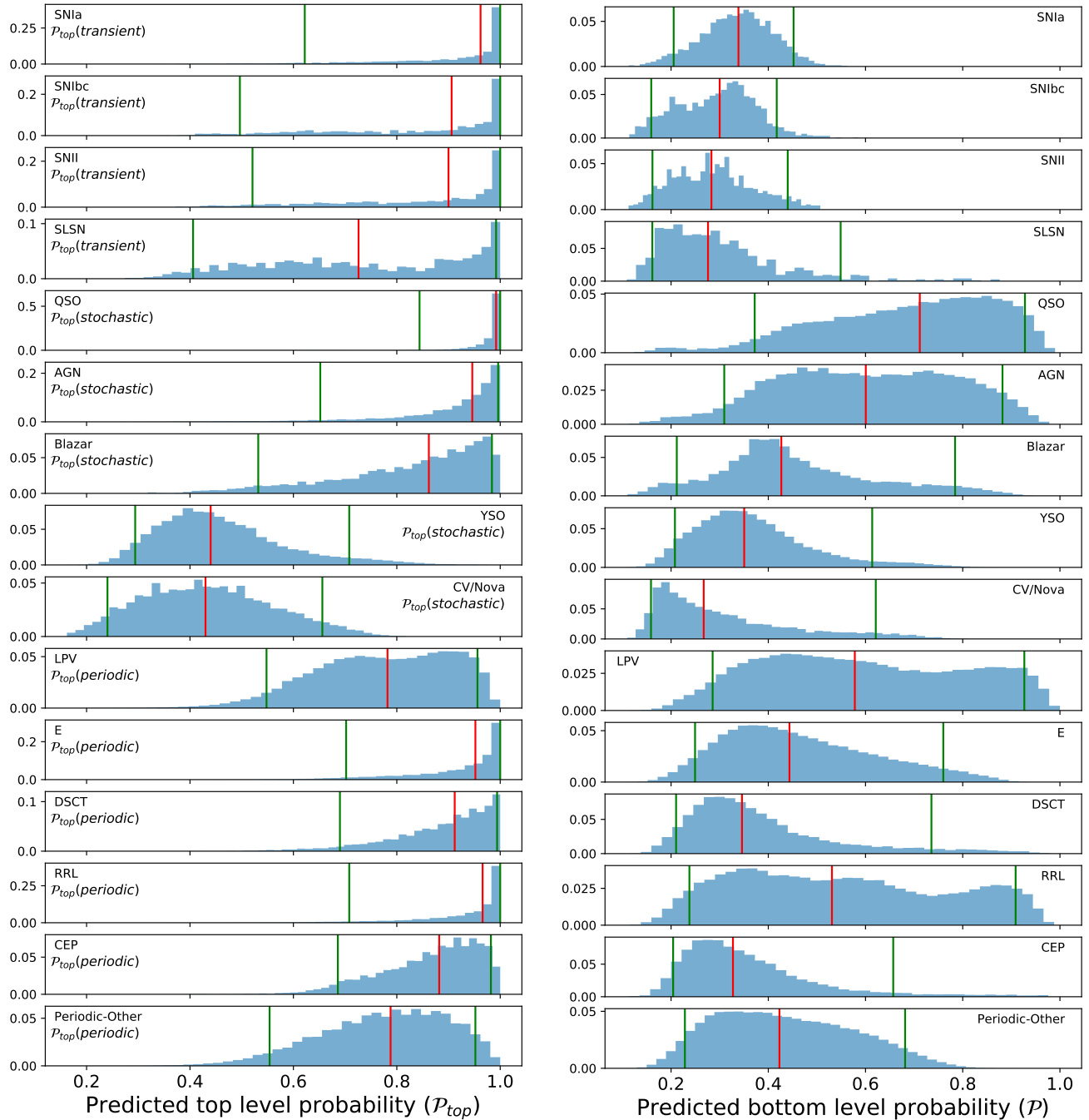
levels on the left and right sides of Figure 13. The red lines denote the position of the median probability for each class, and the green lines denote the 5 and 95 percentiles. It is clear from the figure that the distribution of probabilities for the top level are higher compared to the bottom level. For the top level, the classes with the lowest probabilities are CV/Nova, and YSO. For the bottom level, the classes with the highest probabilities are LPV, QSO, and AGN, and the lowest probabilities are for the different classes of SNe, YSO, CV/Nova, and some periodic variables.

The low probabilities obtained for some classes are related with the confusion between classes observed in Figure 7. For instance, in Figure 7 we can see that the SN classes present a high confusion among them. On the other hand, the SNIa, SNIbc, SNII and SLSN median probabilities of sources classified as SNII are 0.16, 0.19, 0.28 and 0.19, respectively. The high confusion among the SN classes may be due to the low number of sources in the labeled set, but also to the intrinsic similarities among these classes. For example, the physical mechanism responsible for the main peak of the light curve of SNe Ia and SNe Ib/c is the same, the diffusion of energy deposited by radioactive  $^{56}\text{Ni}$  (Arnett 2008). Indeed, Villar et al. (2019a) report that 15% of their Type Ib/c SNe are classified as Ia. This might be improved by performing data augmentation using, for example, Gaussian process modeling (e.g., Boone 2019). On the other hand, the low probabilities observed for CV/Novae and YSOs can be produced by the similarities between their colors and the colors of some periodic sources, and the

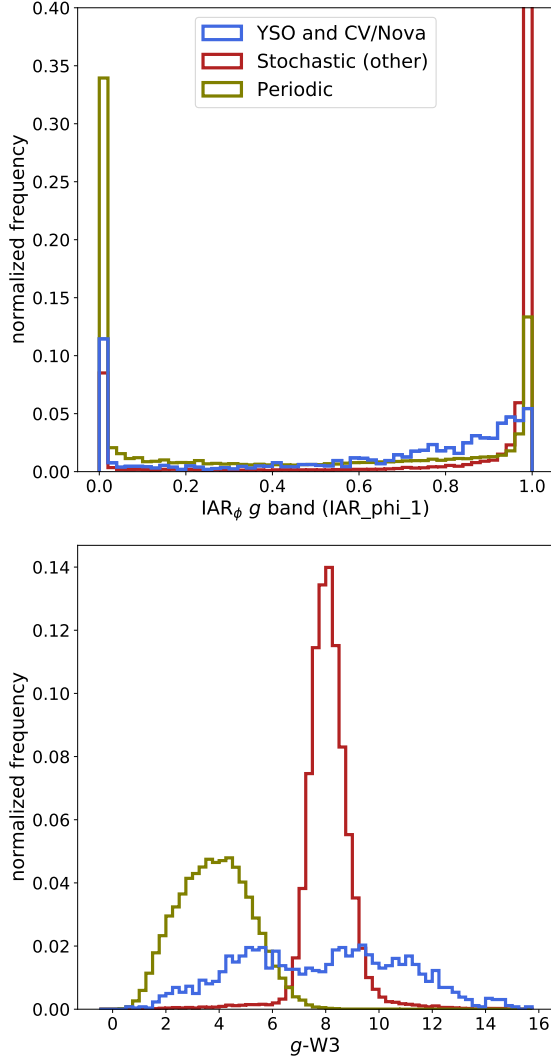
fact that some CV/Novae and YSOs present very rapid variability compared to the ZTF cadence, that produces light curves with low auto-correlation, and thus low values of the `IAR_phi` parameter, which is normally observed for periodic sources (excluding LPVs). These similarities can be seen in Figure 14, where we show the distributions of `IAR_phi_1` and `g-W3` for YSOs and CV/Novae (grouped), the rest of the stochastic classes, and periodic sources from the labeled set.

Figure 15 shows the normalized  $r$  band magnitude distribution of the different classes considering sources present in the labeled set and candidates from the unlabeled ZTF set. In general, the distributions of magnitudes of the candidates are similar to or fainter than found among sources from the labeled set. These results show that the classifier is able to detect faint and bright candidates, regardless of the luminosity biases present in the labeled set, which can be dominated by the brightest tail of the true magnitude distribution of each class.

A simple way to test the performance of the BHRF classifier is to verify whether the results obtained when the model is applied to the unlabeled ZTF set are in agreement with what is astrophysically expected from previous works. For instance, younger Galactic targets like YSOs, Classical Cepheids, and LPVs should reside near the Galactic plane (e.g., Catelan & Smith 2015; Mowlavi et al. 2018), while extragalactic sources like AGNs, QSOs, Blazars, and SNe should have roughly isotropic distributions, perhaps with fewer sources near the Galactic plane due to attenuation/reddening by gas and dust (e.g., Calzetti et al. 2000; Padovani et al. 2017). On the left side of Figure 16 the sky distribution, in Galactic coordinates, of LPV, CEP, and YSO candidates is shown. It is clear from the figure that most of them are located in the Galactic plane, and that sources located outside the plane have a low BHRF probability. This is consistent with the results obtained by previous works (e.g., Mowlavi et al. 2018; Rimoldini et al. 2019). The right panel of Figure 16 shows the Galactic latitude versus the  $g-r$  color obtained using the mean magnitude of the light curves in each band, for extragalactic candidates (QSO, AGN, Blazar, SNIa, SNIbc, SNII, and SLSN). From the figure we can see that the fraction of extragalactic candidates observed around the Galactic plane is low, and that most of the candidates located in the plane have low probabilities. Moreover, the  $g-r$  colors of the extragalactic candidates are consistent with what is expected for these classes, with clear evidence of reddening for the candidates located around the Galactic plane. The sky distribution, in Galactic coordinates, of the extragalactic candidates can be found in Figure 22 of the appendix.



**Figure 13.** Left: normalized probability distributions of the top level of the deployed BHRF classifier, split by subclass, for candidates from the unlabeled ZTF set. The reported values correspond to the probabilities obtained for each class of the top level, as indicated below the class name. Right: normalized probability distributions of the bottom level of the deployed BHRF classifier, split by subclass, for candidates from the unlabeled ZTF set. The red lines show the median probability for each class. The green lines show the 5 and 95 percentiles of the probabilities. Some subclasses show broad distributions to low values, implying that they are not so well-represented or characterized by the highest ranked features within the hierarchical class.



**Figure 14.** Normalized IAR  $\phi$  distribution (*top*) in the  $g$  band (IAR\_phi\_1; cut in the y-axes at 0.4), and normalized  $g$ -W3 distribution (*bottom*), for YSOs and CV/Novae (blue), stochastic sources (red; excluding CV/Novae and YSOs), and periodic sources (yellow). It can be seen that some CV/Novae and YSOs have similar IAR\_phi\_1 and  $g$ -W3 than periodic sources.

## 6. CONCLUSIONS

### 6.1. Summary

In this paper we presented the first version of the ALERCE light curve classifier. This classifier uses a total of 152 features, including variability features computed from ZTF light curves with  $\geq 6$  epochs in  $g$  or  $r$  bands, and colors computed using ZTF and AllWISE photometry (see Section 3), to classify each source into 15 subclasses, including periodic, transient, and stochastic variable sources (see Section 2.2). The light curve classifier uses a balanced hierarchical RF classifier (see

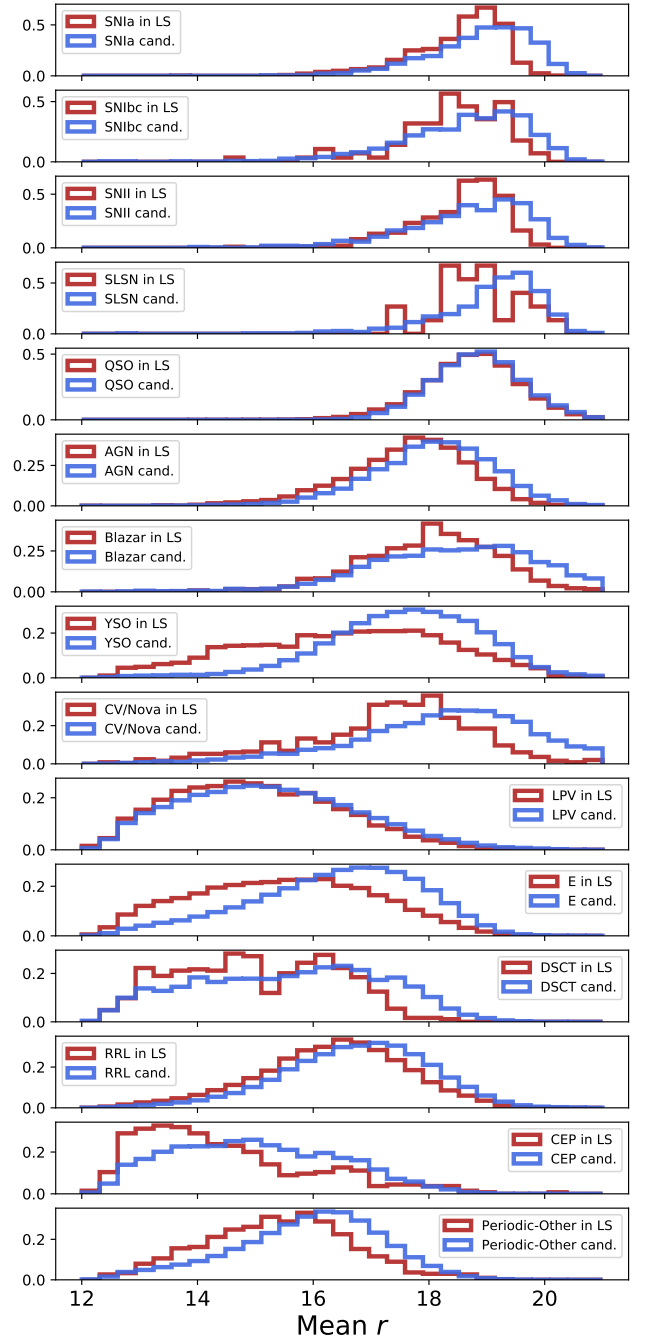


**Figure 15.** Normalized magnitude distributions in the  $r$  band for sources in the labeled set (LS; red histograms) and candidates from the unlabeled ZTF set (cand.; blue histograms).

Section 4.1), constructed with a two-level scheme. The first level (top level) classifies each source as periodic, stochastic or transient. The second level (bottom level) consists of three classifiers that further resolve each hierarchical class into subclasses.

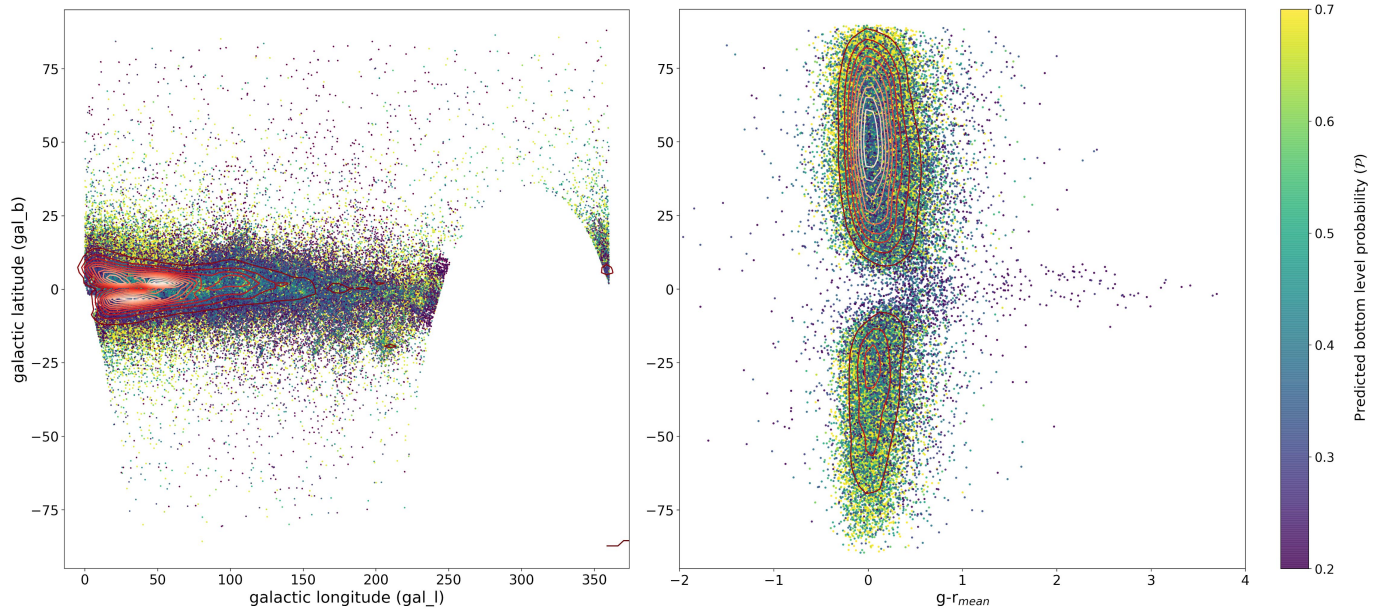


**Figure 16.** Left: Galactic latitude (gal\_b, in degrees) versus Galactic longitude (gal\_l, in degrees) for candidates expected to be mostly observed around the Galactic plane (LPV, CEP, and YSO classes). Right: Galactic latitude (gal\_b, in degrees) versus  $g - r_{max}$  for extragalactic candidates (QSO, AGN, Blazar, SNIa, SNIbc, SNIIf, and SLSN classes). The bottom level probability computed by the deployed BHRF classifier are color-coded according to the colorbar to the right. The red contours show the density of points in each plot. It can be seen that most of the extragalactic candidates are located outside the Galactic plane, while most of the YSO, LPV and CEP candidates are located in the Galactic plane.

We trained and tested the BHRF classifier using a labeled set obtained by cross-matching the ZTF database with different catalogs of transients, stochastic and periodic sources (see Section 2.2.1). For the top level we obtained macro-averaged precision, recall, and F1-score values of 0.96, 0.99, and 0.97, respectively, while for the bottom level we obtained macro-averaged precision, recall, and F1-score values of 0.57, 0.76, and 0.59, respectively.

We used the BHRF classifier to classify 868,371 sources from ZTF (unlabeled ZTF set), obtaining results that are in agreement with what we expect astrophysically. For instance, most of the high probability extragalactic candidates are located outside the Galactic plane, and most of the high probability YSO, LPV, and CEP candidates are located in the Galactic plane (see Figure 16).

The condition of  $\geq 6$  detections in  $g$  or  $r$  normally equates to a timespan between 3 and 30 days since the first detection. Whenever a new detection is received for an object, the ALerCE pipeline processes it and provides an updated classification in  $\sim 1$  second. The light curve classifier provides updated classifications for objects with new ZTF alerts every day. These updated classifications can be found on the [ALerCE Explorer website](#), selecting the “Light curve classifier” option, and specifying the desired class. A catalog con-

taining the features and RF probabilities obtained by the top and bottom levels for the unlabeled ZTF set (up to 2020/06/09) can be downloaded [http://ml.alerce.online/lc\\_pred](http://ml.alerce.online/lc_pred). In addition, more examples and instructions on how to use the ALerCE database and classifications can be found on the [ALerCE Science website](#) and in Förster (2020), and a detailed description of the ALerCE database can be found in the [database schema](#).

## 6.2. Final remarks and perspectives

One of the main challenges found during the development of the ALerCE light curve classifier was the high imbalance present in the labeled set. For instance, the transient sources represent 1.4% of the labeled set, while the periodic sources represent 70.5%. Each hierarchical class also suffers from high imbalance among its subclasses; for example, in the case of the transient class, SNIa comprise 74.0% of the sample, while SLSN correspond to only 1.4%. We addressed this problem by using the balanced RF implementation of the `imbalanced-learn` Python package, which follows the procedure proposed by Chen et al. (2004). This method uses a downsampling majority class technique to train each tree with a balanced sub-sample. We also tested two other algorithms, GBoost and MLP, but concluded that more work is needed if we want to obtain better results from those.

Another challenge was to find features useful to separate the different classes. Previous works have normally used features similar to those available in the FATS Python package (e.g., Kim et al. 2014; Martínez-Palomera et al. 2018), however our first tests demonstrated that these features were not informative enough to separate the 15 classes considered by the light curve classifier, in particular the stochastic and transient classes. Thus, novel features were designed and implemented for this work, like the `IAR_phi` parameter, the MHPS features, and the non-detection features. In addition, during the development of the light curve classifier we realized that some stochastic classes are hard to separate using just variability features. In particular, the separation of YSOs from the other stochastic classes improved significantly once we included AllWISE colors in the set of features (as can be seen in Figures 7 and 9).

Furthermore, the computation of reliable periods was quite challenging, particularly considering that the ALERCE pipeline requires fast computation of features. Huijse et al. (2018) demonstrated that very good results can be achieved by quadratic mutual information (QMI) estimators, however these techniques are computational expensive [ $O(n^2)$ ]. We solve this issue by using the MHAOV periodogram, which provides less reliable periods (see Figure 10 in Huijse et al. 2018), but is much faster to compute [ $O(n)$ ]. Periods become increasingly unreliable as the number of datapoints decreases, but the classification of periodic variables can still be accurate (see RRL, E or LPV panels in Figure 11), as other features can compensate for the decreasing quality of the periodogram (e.g., features related with the amplitude and the timescale of the variability). ALERCE is currently working to implement methods for period estimation that are both accurate and fast. Computing the periodogram is expensive for sources with a large number of detections. We are currently exploring so-called “online” periodograms, which are updated as new samples arrive, at a fraction of the computational cost of recomputing the period each time from scratch (Zorich et al. 2020), as well as other techniques that might work better with eclipsing binary light curves (e.g., Kovács et al. 2002; Mighell & Plavchan 2013).

Moreover, the classification of the different SN classes was particularly challenging. First, the number of SNe in the labeled set was very small compared to other classes, and second, the light curves of SN classes can present similarities, which makes their separation difficult, as discussed in Section 5.3.2. We solved this issue by using the `BalancedRandomForestClassifier` method from `imbalanced-learn`, and by including the SPM features, whose definition is a modification of the

work of Villar et al. (2019a). In the future we plan to test other techniques to improve the separation of SN classes. Previous works have performed Gaussian process regression to model SNe light curves and generate new light curves with different cadences therefrom (e.g., Boone 2019). Moreover, better results can be obtained if we use information regarding the SN host galaxy (e.g. Foley & Mandel 2013; Baldeschi et al. 2020).

In the future we also plan to perform data augmentation to improve the classification of persistent variable objects. For the case of variable stars, light curves can be modeled with Gaussian process or with a combination of harmonics, and then basic transformations can be applied to these models to obtain light curves with different periods and amplitudes (e.g., Elorrieta et al. 2016; Martínez-Palomera et al. 2018; Castro et al. 2018; Aguirre et al. 2019). To the best of our knowledge for the case of AGNs, QSOs and Blazars no previous attempts to perform data augmentation have been made. A promising option is to use synthetic light curve generators that consider the physical processes behind the variability (e.g., Sartori et al. 2019).

Most of the features used by this classifier can be implemented and used to classify light curves from other data sets. In particular, for the case of LSST, the non-detection features can be adapted to work with the forced photometry that will be provided for each alert (`DIAForcedSources` in the Data Products Definition Document; Jurić et al. 2019). LSST will also benefit from the multiband *ugrizy* light curves. As we demonstrated in this work, in general the light curve classification improves when both ZTF *g* and *r* data are available. For the case of LSST this would be the same, and probably we should even be able to further resolve some of the subclasses presented in this work. For instance, using the *zy* light curves we should be able to separate local type 1 and type 2 active galactic nuclei, since for low redshift sources, we can detect variability from the dusty torus at these wavelengths (see Sánchez et al. 2017 and references therein), or identify high redshift QSOs, whose emission is expected to be absorbed in the bluer bands. We encourage researches interested in classifying stochastic and transient sources in particular to use the novel (or modified) features presented in this work, like the `IAR_phi` parameter, the MHPS features, the SPM features, and the non-detection features.

It is worth to note that the ALERCE light curve classifier is being constantly improved, and this work describes its Version 1.0. Future versions of this classifier may include new classes of variable and transient objects, as well as sub-classes of sources already present in the taxonomy (e.g., RRL types ab and c; classical

and type II CEPs; contact, detached, and semi-detached eclipsing binaries; among others). We are also working to find new features and techniques that can improve the performance of the classifier. Future work will report any changes included in the classifier model, like the inclusion of data augmentation, or the use of other classification strategies (e.g., semi supervised training). We recommend the users of this classifier to check the [ALeRCE Science website](#) to get updates related with the different classifiers and the data processing. We are exploring different classification algorithms which are not based on manually designed features, but on automatically derived, recurrent, implicitly extracted features, via deep learning (e.g. [Naul et al. 2018](#); [Muthukrishna et al. 2019](#); [Becker et al. 2020](#)). However, up to this point we have found that the former produce better results when applied to real data. Most likely, a combination of simulated and real data will be required to train reliable deep learning classification models in the future, as found by [Carrasco-Davis et al. \(2019\)](#).

#### ACKNOWLEDGMENTS

The authors acknowledge support from: ANID Millennium Science Initiative ICN12.009; ANID grants PIA AFB-170001 (F.F., I.R., C.V., E.C., D.R., L.S.G., C.S.C., D.R.U.), PIA ACT172033 (P.A.), Basal-CATA AFB-170002 (P.S.S., F.E.B., M.C., D.D.), FONDECYT Regular N 1200710 (F.F.), 1190818 (F.E.B.), 1200495 (F.E.B.), 1171678 (P.E.) and 1171273 (M.C.), FONDECYT Initiation N 11191130 (G.C.V.), and FONDECYT Postdoctorado N 3200250 (P.S.S.), and 3200222 (D.D.), the Max-Planck Society, Germany, through a Partner Group grant (P.A.). Powered@NLHPC: This research was partially supported by the supercomputing infrastructure of the NLHPC (ECM-02).

Based on observations obtained with the Samuel Oschin 48-inch Telescope at the Palomar Observatory

as part of the Zwicky Transient Facility project. ZTF is supported by the National Science Foundation under Grant No. AST-1440341 and a collaboration including Caltech, IPAC, the Weizmann Institute for Science, the Oskar Klein Center at Stockholm University, the University of Maryland, the University of Washington, Deutsches Elektronen-Synchrotron and Humboldt University, Los Alamos National Laboratories, the TANGO Consortium of Taiwan, the University of Wisconsin at Milwaukee, and Lawrence Berkeley National Laboratories. Operations are conducted by COO, IPAC, and UW. AllWISE makes use of data from WISE, which is a joint project of the University of California, Los Angeles, and the Jet Propulsion Laboratory/California Institute of Technology, and NEOWISE, which is a project of the Jet Propulsion Laboratory/California Institute of Technology. WISE and NEOWISE are funded by the National Aeronautics and Space Administration.

*Software:* Apache Kafka<sup>4</sup>, Apache Spark ([Zaharia et al. 2016](#)), ASTROIDE ([Brahem et al. 2020](#)), Astropy ([Astropy Collaboration et al. 2013, 2018](#)), Dask ([Rocklin 2015](#)), FATS ([Nun et al. 2015](#)), IAR<sup>5</sup> ([Eyheramendy et al. 2018](#)), Imbalanced-learn ([Lemaître et al. 2017](#)), Jupyter ([Kluyver et al. 2016](#)), Keras ([Chollet et al. 2015](#)), Matplotlib ([Hunter 2007](#)), Numpy & Scipy ([van der Walt et al. 2011](#)), P4J ([Huijse et al. 2018](#)), Pandas ([McKinney et al. 2010](#)), PostgreSQL<sup>6</sup>, Python ([Van Rossum & Drake Jr 1995](#)), Scikit-learn ([Pedregosa et al. 2012](#)), Seaborn ([Waskom et al. 2017](#)), Tensorflow ([Abadi et al. 2016](#)), TOPCAT ([Taylor 2005](#)), XGBoost ([Chen & Guestrin 2016](#)).

#### APPENDIX

##### A. FURTHER DESCRIPTION OF SOME VARIABILITY FEATURES

In this section we provide additional description of some of the features listed in Table 2 (those marked with \*\*). These features correspond to new variants of features included in the FATS package and other works:

- Damp Random Walk (DRW) parameters: a DRW model is defined by a stochastic differential equation which includes a damping term that pushes the signal back to its mean:  $dX(t) = -\frac{1}{\tau_{DRW}}X(t)dt + \sigma_{DRW}\sqrt{dt}\epsilon(t) +$

<sup>4</sup> <https://kafka.apache.org/>

<sup>5</sup> Python and R implementations are available in [https://github.com/felipeelorrjeta/IAR\\_Model](https://github.com/felipeelorrjeta/IAR_Model)

<sup>6</sup> <https://www.postgresql.org/>

$b dt$ ,  $\tau_{DRW}, \sigma_{DRW}, t > 0$ .  $\tau_{DRW}$  corresponds to the characteristic time for the time series to become roughly uncorrelated,  $\sigma_{DRW}$  corresponds to the amplitude of the variability at short timescales ( $t \ll \tau_{DRW}$ ), and  $\epsilon(t)$  is a white noise process with zero mean and variance equal to 1. DRW modelling is typically used to describe light curves of active galactic nuclei (Kelly et al. 2009). In this case we obtained the  $\sigma_{DRW}$  and  $\tau_{DRW}$  parameters using Gaussian process regression, with a Ornstein-Uhlenbeck kernel, as in Graham et al. (2017). `GP_DRW_sigma` denotes  $\sigma_{DRW}$ , while `GP_DRW_tau` denotes  $\tau_{DRW}$ .

- **Excess Variance ( $\sigma_{\text{rms}}$ ):** Measure of the intrinsic variability amplitude in a given band (see Sánchez et al. 2017, and references therein).  $\sigma_{\text{rms}}^2 = (\sigma_{LC}^2 - \bar{\sigma}_m^2) / \bar{m}^2$ , where  $\sigma_{LC}$  is the standard deviation of the light curve,  $\bar{\sigma}_m$  is the average photometric error, and  $\bar{m}$  is the average magnitude. We denoted  $\sigma_{\text{rms}}^2$  as `ExcessVar`.
- **$P_{\text{var}}$ :** Probability that the source is intrinsically variable in a given band (see Paolillo et al. 2004, and references therein). It considers the  $\chi^2$  of the light curve respect to its mean, and calculates the probability  $P_{\text{var}} = P(\chi^2)$  that a  $\chi^2$  lower or equal to the observed value could occur by chance for an intrinsically non-variable source, assuming that for each light curve its  $\chi^2$  will follow a probability distribution described by an incomplete gamma function  $\Gamma(\nu/2, \chi^2/2)$ , where  $\nu$  corresponds to the degrees of freedom. We denoted  $P_{\text{var}}$  as `Pvar`.
- **Structure Function (SF) parameters:** The SF quantifies the amplitude of the variability as a function of the time difference between pairs of detections ( $\tau$ ). In this work we consider the definition provided by Caplar et al. (2017). We model the SF as a power law:  $\text{SF}(\tau) = A_{\text{SF}} \left(\frac{\tau}{1\text{yr}}\right)^{\gamma_{\text{SF}}}$ , where  $\gamma_{\text{SF}}$  corresponds to the logarithmic gradient of the change in magnitude, and  $A_{\text{SF}}$  corresponds to the amplitude of the variability at 1 yr. `SF_ML_amplitude` denotes  $A_{\text{SF}}$ , while `SF_ML_gamma` denotes  $\gamma_{\text{SF}}$ .

## B. ONE-LEVEL MULTI-CLASS RF MODEL

The first model tested for the ALERCE light curve classifier was a simple one-level RF model with 15 classes, implemented using the `imbalanced-learn` Python package. This model uses 500 trees, maximum depth trees, and maximum number of features equal to the square root of the total number of features. Figure 17 shows the confusion matrix obtained by this model. The precision, recall and F1-score obtained are 0.49, 0.68, and 0.50, respectively. Clearly this model has a lower performance compared to the BHRF classifier.

## C. THE PARTICULAR CASE OF RRL

In Section 5.2 we claimed that the low recall values obtained in the  $g$  band for bright RRL can be explained by the differences in the variability features of the RRL sub-types. Figure 18 shows the `Multiband_period` versus the `Meanvariance` measured in the  $g$  and  $r$  bands, for RRLs split into their sub-classes ‘ab’ and ‘c’, and for E, CEP, and DSCT (grouped as a single class). From the figure we can notice that ab-type RRL tend to have larger `Meanvariance` in the  $g$  band, which helps to distinguish them from E/CEP/DSCT, while c-type RRL have values of `Meanvariance` in both bands similar to those of E/CEP/DSCT, which makes it difficult to tell them apart. The RRL class in our labeled set is dominated by ab-type RRL ( $\sim 80\%$ ), and thus the light curve classifier identifies those more easily. However, for bright sources ( $g \leq 15$ ), the fraction of ab-type RRL decreases to 64%, which explains the low recall values obtained for this regime of brightness.

## D. THE PARTICULAR CASE OF AGN, QSO AND BLAZAR

In this work we present the first attempt to separate different types of active galactic nuclei according to their variability properties. As we mentioned in Section 2.2, we separate active galactic nuclei in the following way:

- **AGN:** type 1 Seyfert galaxies (i.e., active galactic nuclei whose emission is dominated by the host galaxy), selected from MILLIQUAS (broad type “A”), and from Oh et al. (2015).
- **QSO:** type 1 nucleus-dominated active galactic nuclei (i.e., active galactic nuclei whose emission is dominated by their active nuclei), selected from MILLIQUAS (broad type “Q”).
- **Blazar:** BL Lac objects and Flat Spectrum Radio Quasars (FSRQ), selected from ROMABZCAT and MILLIQUAS.

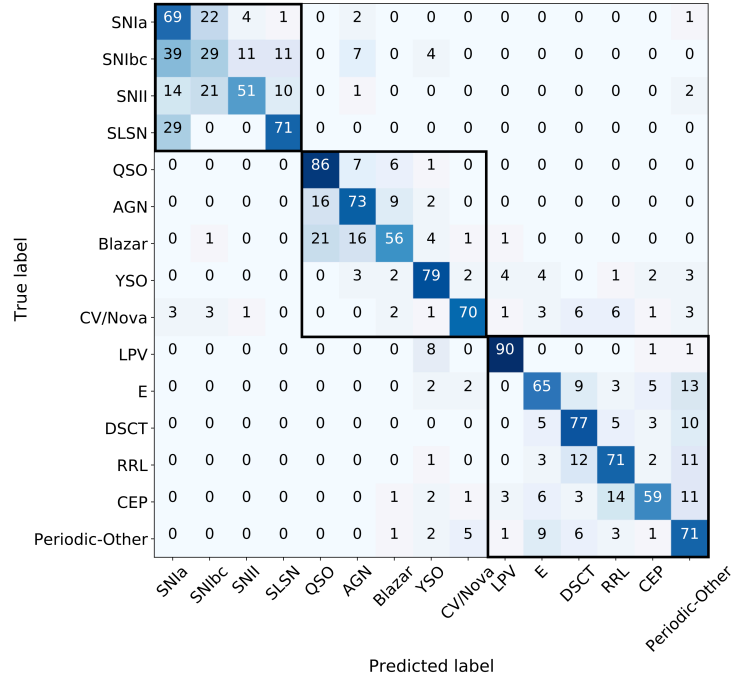


**Figure 17.** Confusion matrix for a one-level multi-class RF Model. The black squares highlight the three hierarchical classes (from top to bottom, transient, stochastic, and periodic, respectively). The reported values correspond to the percentages obtained by normalizing the matrix with the true labels. The performance of this model is poorer compared to the BHRF classifier (see Figure 7).

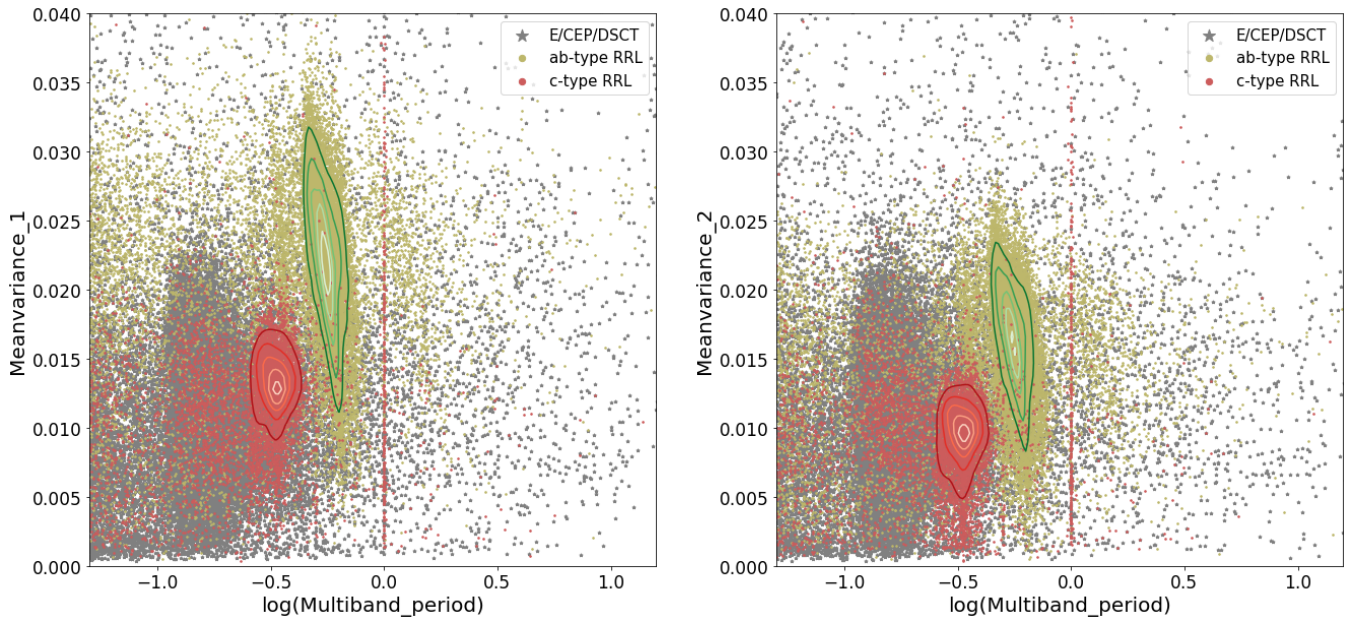


**Figure 18.** Logarithm of the Multiband period versus the Meanvariance<sub>1</sub> (*g* band, left) and the Meanvariance<sub>2</sub> (*r* band, right), for RRL split according to their sub-classes ‘ab’ (green) and ‘c’ (red), and for E, CEP, and DSCT (grey). We show a zoom in the area where most of the RRLs lie. The contours show the density of points of each RRL class.

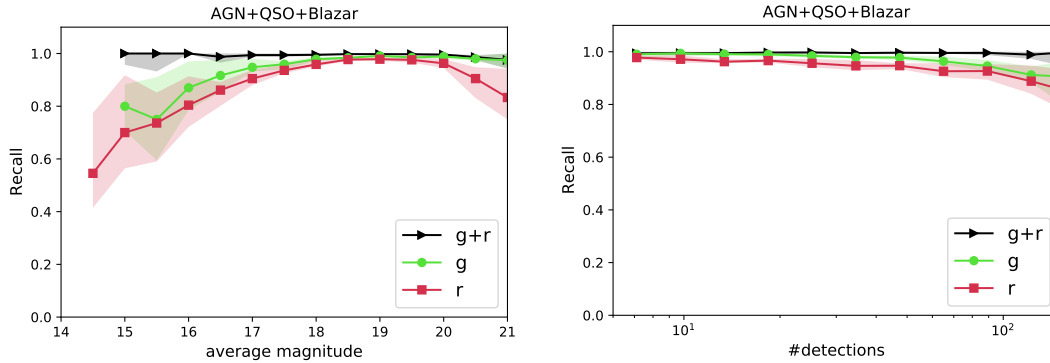


**Figure 19.** Similar to Figures 10 and 11, but treating AGNs, QSOs, and Blazars as a single class. When grouped together, the recall is much better behaved than for any individual active galactic nuclei class, highlighting remaining difficulties distinguishing between these classes.

In Figure 11 we showed the recall curves for each class as a function of the number of detections, and we could observe that these curves decrease for QSOs and AGNs when more detections are available, particularly in the  $r$  band. These results are puzzling, considering that we would normally expect to improve the classification of a given class as more detections are included in the light curves. In order to better understand the origin of these results, we show in Figure 19 the recall curves as a function of average magnitude and number of detections for AGNs, QSOs and Blazars grouped as a single class. In this case, the recall curves are around 0.8 and 1.0 for every bin of magnitude (specially for  $g > 16$  or  $r > 16$ ) and number of detections. From this we can infer that the light curve classifier has a very good performance selecting active galactic nuclei as a single class, but some issues still remain regarding the separation of AGNs, QSOs, and Blazars. There are two main explanations for these results: a) the method cannot properly separate QSOs from AGNs and Blazars, or b) there are sources in the labeled set with incorrect labels.

A possible way to explore how well the light curve classifier can discriminate among AGNs, QSOs, and Blazars, is to check whether the features available in the light curve classifier can separate these three populations. Figure 20 shows six different features used by the classifier,  $(g-r)_{\text{mean\_corr}}$ ,  $\text{Meanvariance}_1$ ,  $\text{ExcessVar}_1$ ,  $\text{sgscore}_1$ ,  $\text{Meanvariance}_2$ , and  $\text{ExcessVar}_2$ , for QSOs, AGNs, and Blazars from the labeled set (most of these features are in the top 30-ranked features shown in Table 6). From the figure we can see that these three classes have different color distributions, different morphologies, and also different variability properties. AGNs and Blazars tend to be redder than QSOs (see  $(g-r)_{\text{mean\_corr}}$ ), Blazars and AGNs tend to have larger amplitudes (see  $\text{Meanvariance}_1$  and  $\text{ExcessVar}_1$ ), and AGNs tend to have more extended morphologies compared to QSOs and Blazars. These are just some examples of features that can be used to separate the three classes above mentioned. After a visual inspection of the feature distribution of AGNs, QSOs, and Blazars, we found that more than 30 features can be used to separate them, including for instance  $\text{PercentileAmplitude}$ ,  $\text{Q31}$ ,  $\text{GP\_DRW\_sigma}$ ,  $\text{GP\_DRW\_tau}$ ,  $\text{MHPS\_low}$ ,  $\text{MHPS\_high}$ ,  $\text{SF\_ML\_amplitude}$ , among others. From this we can infer that the light curve classifier should be able to separate these three populations properly.

In addition, from Figure 20 we can notice that for the case of AGNs and QSOs, the distribution of features obtained using the  $g$  band light curves presents larger differences compared to the features obtained for the  $r$  band. This behavior is also seen in other features, like  $\text{PercentileAmplitude}$ ,  $\text{GP\_DRW\_sigma}$ ,  $\text{Std}$ , among other features related with the amplitude of the variability. These differences might be produced by the combined effect of having a higher contamination from the host in the  $r$  band and intrinsically lower amplitude of the variability in the  $r$  band, due to the well known anti-correlation between amplitude of the variability and the wavelength of emission (see Sánchez et al. 2017 and references therein). From this, we can understand the differences observed in the  $g$  and  $r$  band recall curves of AGNs and QSOs shown in Figure 11, which should be produced by these differences in the features distributions.

On the other hand, MILLIQUAS uses a luminosity-based divider to separate AGNs and QSOs (see Section 5 of Flesch 2015), and therefore we expect that a fraction of sources could have an incorrect classification, if the host galaxy component is not corrected properly. In order to see whether there are sources in the labeled set with incorrect QSO or AGN classification, we crossmatched our labeled set with the SIMBAD database. There are 26168 QSOs in the labeled set (all obtained from MILLIQUAS), and 1590 of them are classified as Seyfert or AGN by SIMBAD

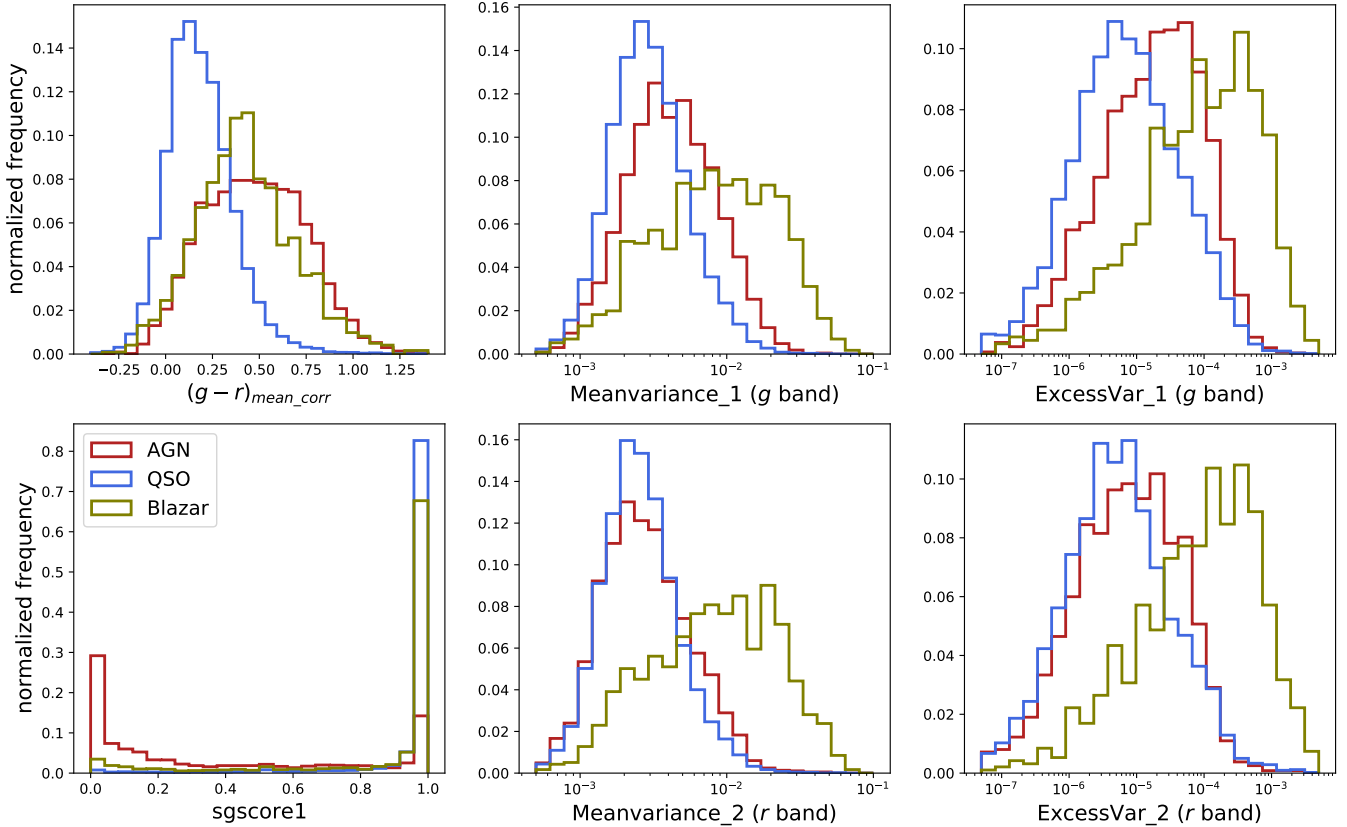


**Figure 20.** Distribution of  $(g-r)_{\text{mean\_corr}}$ ,  $\text{Meanvariance}_1$ ,  $\text{ExcessVar}_1$ ,  $\text{sgscore1}$ ,  $\text{Meanvariance}_2$ , and  $\text{ExcessVar}_2$ , for QSOs (blue), AGNs (red), and Blazars (yellow) classes from the labeled set. These features (among others) can be used to separate these classes of active galactic nuclei.

(6%), with 1580 having a reported redshift  $< 1$ . On the other hand, there are 4667 AGNs in the labeled set, and 830 (17%) of them are classified as QSO in SIMBAD. Therefore, there are 2420 sources in the labeled set with inconsistent classification in MILLIQUAS and SIMBAD. The light curve classifier classifies 920 of these sources as QSO and 1319 as AGN. To understand more properly the differences between these AGN and QSO candidates, we plot in Figure 21 the same features plotted in Figure 20 for the sources with inconsistent classification in MILLIQUAS and SIMBAD, splitting them according to their predicted class from the BHRF model. The distribution of features of these AGN and QSO candidates is similar to the general distributions observed for AGNs and QSOs from the labeled set. Again, AGNs tend to have higher variability amplitudes, redder colors and extended morphologies.

From these results, we can infer that the decrease in the recall as a function of the number of detections observed for QSOs and AGNs is produced by the discrepancy in the QSO/AGN classification obtained from different catalogs. When more epochs are available, it is easier for the light curve classifier to perform a correct variability-based classification, and therefore, identify an original incorrect classification provided by a given catalog. We propose that by using the variability properties of active galactic nuclei we can more easily separate them as nucleus-dominated or host-dominated, or in other words, as regular QSOs or low luminosity AGNs.

### E. SKY DISTRIBUTION OF THE EXTRAGALACTIC CANDIDATES

Figure 22 shows the sky distribution (in Galactic coordinates) of extragalactic candidates (QSO, AGN, Blazar, SNIa, SNIbc, SNII, and SLSN). It is expected that only a few extragalactic candidates are observed in the Galactic plane, which is confirmed in Figure 22.

### REFERENCES

- Abadi, M., Barham, P., Chen, J., et al. 2016, in 12th {USENIX} Symposium on Operating Systems Design and Implementation ({OSDI} 16), 265–283
- Abril, J., Schmidtobreick, L., Ederoclite, A. r., & López-Sanjuan, C. 2020, MNRAS, 492, L40, doi: [10.1093/mnras/slz181](https://doi.org/10.1093/mnras/slz181)

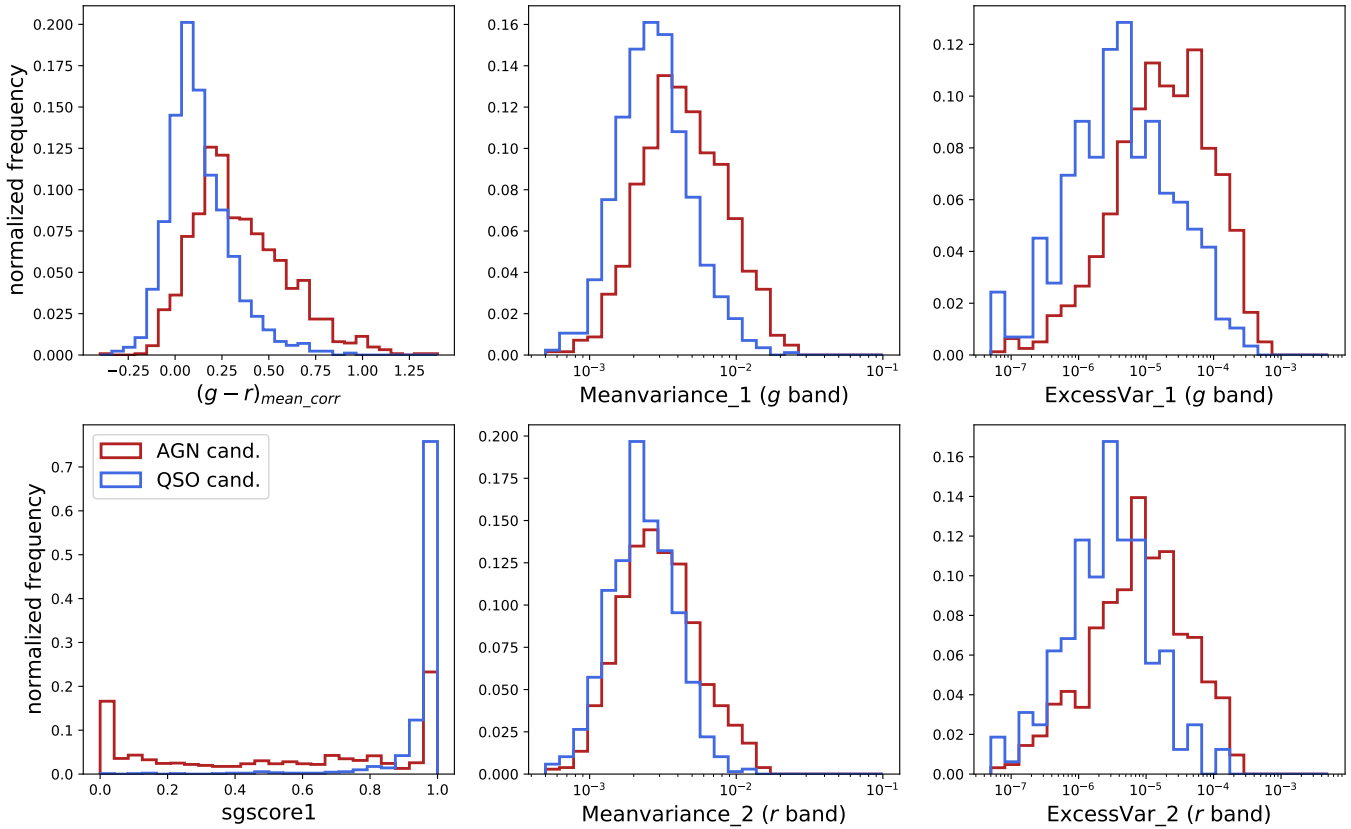


**Figure 21.** Distribution of  $(g-r)_{\text{mean\_corr}}$ ,  $\text{Meanvariance}_1$ ,  $\text{ExcessVar}_1$ ,  $\text{sgscore1}$ ,  $\text{Meanvariance}_2$ , and  $\text{ExcessVar}_2$ , for sources from the labeled set with discrepancies in their classification according to MILLIQUAS and SIMBAD, and classified as AGN (red) and QSO (blue) by the light curve classifier. The distribution of features is similar to that presented in Figure 20 for QSOs and AGNs.

Aguirre, C., Pichara, K., & Becker, I. 2019, MNRAS, 482, 5078, doi: [10.1093/mnras/sty2836](https://doi.org/10.1093/mnras/sty2836)

Allevato, V., Paolillo, M., Papadakis, I., & Pinto, C. 2013, ApJ, 771, 9, doi: [10.1088/0004-637X/771/1/9](https://doi.org/10.1088/0004-637X/771/1/9)

Arévalo, P., Churazov, E., Zhuravleva, I., Hernández-Monteagudo, C., & Revnivtsev, M. 2012, MNRAS, 426, 1793, doi: [10.1111/j.1365-2966.2012.21789.x](https://doi.org/10.1111/j.1365-2966.2012.21789.x)

Arnett, D. 2008, in American Institute of Physics Conference Series, Vol. 1053, American Institute of Physics Conference Series, ed. S. K. Chakrabarti & A. S. Majumdar, 237–242, doi: [10.1063/1.3009489](https://doi.org/10.1063/1.3009489)

Astropy Collaboration, Robitaille, T. P., Tollerud, E. J., et al. 2013, A&A, 558, A33, doi: [10.1051/0004-6361/201322068](https://doi.org/10.1051/0004-6361/201322068)

Astropy Collaboration, Price-Whelan, A. M., Sipőcz, B. M., et al. 2018, AJ, 156, 123, doi: [10.3847/1538-3881/aabc4f](https://doi.org/10.3847/1538-3881/aabc4f)

Baldeschi, A., Miller, A., Stroh, M., Margutti, R., & Coppejans, D. L. 2020, arXiv e-prints, arXiv:2005.00155. <https://arxiv.org/abs/2005.00155>

Becker, I., Pichara, K., Catelan, M., et al. 2020, MNRAS, 493, 2981, doi: [10.1093/mnras/staa350](https://doi.org/10.1093/mnras/staa350)

Bellm, E. 2014, in The Third Hot-wiring the Transient Universe Workshop, ed. P. R. Wozniak, M. J. Graham, A. A. Mahabal, & R. Seaman, 27–33. <https://arxiv.org/abs/1410.8185>

Bellm, E. C., Kulkarni, S. R., Graham, M. J., et al. 2019, PASP, 131, 018002, doi: [10.1088/1538-3873/aaecbe](https://doi.org/10.1088/1538-3873/aaecbe)

Ben-Israel, A., & Greville, T. 2003, Adi Ben-Israel and Thomas N.E. Greville, Generalized Inverses: Theory and Applications, ISBN 0-387-00293-6, doi: <https://doi.org/10.1007/b97366>

Boone, K. 2019, AJ, 158, 257, doi: [10.3847/1538-3881/ab5182](https://doi.org/10.3847/1538-3881/ab5182)

Brahem, M., Zeitouni, K., & L., Y. 2020, ApJ

Breiman, L. 2001, Machine Learning, 45, 5, doi: [10.1023/A:1010933404324](https://doi.org/10.1023/A:1010933404324)

Butler, N. R., & Bloom, J. S. 2011, AJ, 141, 93, doi: [10.1088/0004-6256/141/3/93](https://doi.org/10.1088/0004-6256/141/3/93)

Calzetti, D., Armus, L., Bohlin, R. C., et al. 2000, ApJ, 533, 682, doi: [10.1086/308692](https://doi.org/10.1086/308692)

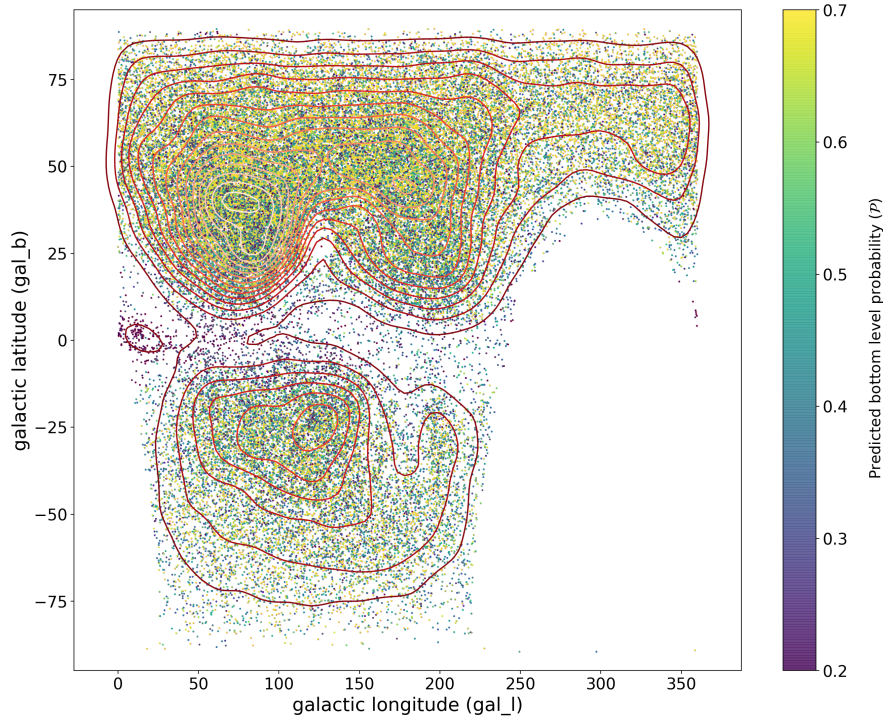


**Figure 22.** Galactic latitude (gal\_b, in degrees) versus Galactic longitude (gal\_l, in degrees) for extragalactic candidates (QSO, AGN, Blazar, SNIa, SNIbc, SNII, and SLSN classes). The contours show the density of points in the plot. The bottom level probability computed by the deployed BHRF classifier are color-coded according to the color bar to the right.

- Caplar, N., Lilly, S. J., & Trakhtenbrot, B. 2017, *ApJ*, 834, 111, doi: [10.3847/1538-4357/834/2/111](https://doi.org/10.3847/1538-4357/834/2/111)
- Carrasco-Davis, R. 2020, *AJ*
- Carrasco-Davis, R., Cabrera-Vives, G., Förster, F., et al. 2019, *PASP*, 131, 108006, doi: [10.1088/1538-3873/aaef12](https://doi.org/10.1088/1538-3873/aaef12)
- Castro, N., Protopapas, P., & Pichara, K. 2018, *AJ*, 155, 16, doi: [10.3847/1538-3881/aa9ab8](https://doi.org/10.3847/1538-3881/aa9ab8)
- Catelan, M., Dekany, I., Hempel, M., & Minniti, D. 2013, *Boletín de la Asociación Argentina de Astronomía La Plata Argentina*, 56, 153
- Catelan, M., & Smith, H. A. 2015, *Pulsating Stars* (Wiley-VCH, Weinheim)
- Chambers, K. C., Magnier, E. A., Metcalfe, N., et al. 2016, arXiv e-prints, arXiv:1612.05560. <https://arxiv.org/abs/1612.05560>
- Chen, C., Liaw, A., Breiman, L., et al. 2004, University of California, Berkeley, 110, 24
- Chen, T., & Guestrin, C. 2016, in *Proceedings of the 22nd ACM SIGKDD International Conference on Knowledge Discovery and Data Mining, KDD '16* (New York, NY, USA: ACM), 785–794, doi: [10.1145/2939672.2939785](https://doi.org/10.1145/2939672.2939785)
- Chollet, F., et al. 2015, *Keras*, <https://keras.io>
- De Cicco, D., Paolillo, M., Falocco, S., et al. 2019, *A&A*, 627, A33, doi: [10.1051/0004-6361/201935659](https://doi.org/10.1051/0004-6361/201935659)
- Debosscher, J., Sarro, L. M., Aerts, C., et al. 2007, *A&A*, 475, 1159, doi: [10.1051/0004-6361:20077638](https://doi.org/10.1051/0004-6361:20077638)
- Debosscher, J., Sarro, L. M., López, M., et al. 2009, *A&A*, 506, 519, doi: [10.1051/0004-6361/200911618](https://doi.org/10.1051/0004-6361/200911618)
- D’Isanto, A., Cavuoti, S., Brescia, M., et al. 2016, *MNRAS*, 457, 3119, doi: [10.1093/mnras/stw157](https://doi.org/10.1093/mnras/stw157)
- Drake, A. J., Djorgovski, S. G., Mahabal, A., et al. 2009, *ApJ*, 696, 870, doi: [10.1088/0004-637X/696/1/870](https://doi.org/10.1088/0004-637X/696/1/870)
- Drake, A. J., Graham, M. J., Djorgovski, S. G., et al. 2014, *ApJS*, 213, 9, doi: [10.1088/0067-0049/213/1/9](https://doi.org/10.1088/0067-0049/213/1/9)
- Drake, A. J., Djorgovski, S. G., Catelan, M., et al. 2017, *MNRAS*, 469, 3688, doi: [10.1093/mnras/stx1085](https://doi.org/10.1093/mnras/stx1085)
- Elorrieta, F., Eyheramendy, S., Jordán, A., et al. 2016, *A&A*, 595, A82, doi: [10.1051/0004-6361/201628700](https://doi.org/10.1051/0004-6361/201628700)
- Eyheramendy, S., Elorrieta, F., & Palma, W. 2018, *MNRAS*, 481, 4311, doi: [10.1093/mnras/sty2487](https://doi.org/10.1093/mnras/sty2487)
- Flesch, E. W. 2015, *PASA*, 32, e010, doi: [10.1017/pasa.2015.10](https://doi.org/10.1017/pasa.2015.10)
- . 2019, arXiv e-prints, arXiv:1912.05614. <https://arxiv.org/abs/1912.05614>
- Foley, R. J., & Mandel, K. 2013, *ApJ*, 778, 167, doi: [10.1088/0004-637X/778/2/167](https://doi.org/10.1088/0004-637X/778/2/167)
- Förster, F. 2020, *AJ*
- Förster, F., Maureira, J. C., San Martín, J., et al. 2016, *ApJ*, 832, 155, doi: [10.3847/0004-637X/832/2/155](https://doi.org/10.3847/0004-637X/832/2/155)
- Förster, F., Moriya, T. J., Maureira, J. C., et al. 2018, *Nature Astronomy*, 2, 808, doi: [10.1038/s41550-018-0563-4](https://doi.org/10.1038/s41550-018-0563-4)

- Friedman, J. H. 2001, *Annals of statistics*, 1189
- Graham, M. J., Djorgovski, S. G., Drake, A. J., et al. 2017, *MNRAS*, 470, 4112, doi: [10.1093/mnras/stx1456](https://doi.org/10.1093/mnras/stx1456)
- Graham, M. J., Drake, A. J., Djorgovski, S. G., et al. 2013, *MNRAS*, 434, 3423, doi: [10.1093/mnras/stt1264](https://doi.org/10.1093/mnras/stt1264)
- Guillochon, J., Parrent, J., Kelley, L. Z., & Margutti, R. 2017, *ApJ*, 835, 64, doi: [10.3847/1538-4357/835/1/64](https://doi.org/10.3847/1538-4357/835/1/64)
- Hastie, T., Tibshirani, R., & Friedman, J. 2009, *The Elements of Statistical Learning: Data Mining, Inference, and Prediction*, Springer series in statistics (Springer). <https://link.springer.com/book/10.1007/978-0-387-84858-7>
- Haykin, S. 1994, *Neural networks: a comprehensive foundation* (Prentice Hall PTR)
- Holoien, T. W. S., Brown, J. S., Valley, P. J., et al. 2019, *MNRAS*, 484, 1899, doi: [10.1093/mnras/stz073](https://doi.org/10.1093/mnras/stz073)
- Huijse, P., Estévez, P. A., Förster, F., et al. 2018, *ApJS*, 236, 12, doi: [10.3847/1538-4365/aab77c](https://doi.org/10.3847/1538-4365/aab77c)
- Hunter, J. D. 2007, *Computing in Science Engineering*, 9, 90
- Ivezić, Ž., Kahn, S. M., Tyson, J. A., et al. 2019, *ApJ*, 873, 111, doi: [10.3847/1538-4357/ab042c](https://doi.org/10.3847/1538-4357/ab042c)
- Jayasinghe, T., Kochanek, C. S., Stanek, K. Z., et al. 2018, *MNRAS*, 477, 3145, doi: [10.1093/mnras/sty838](https://doi.org/10.1093/mnras/sty838)
- Jayasinghe, T., Stanek, K. Z., Kochanek, C. S., et al. 2019a, *MNRAS*, 486, 1907, doi: [10.1093/mnras/stz844](https://doi.org/10.1093/mnras/stz844)
- . 2019b, *MNRAS*, 485, 961, doi: [10.1093/mnras/stz444](https://doi.org/10.1093/mnras/stz444)
- . 2020, *MNRAS*, 491, 13, doi: [10.1093/mnras/stz2711](https://doi.org/10.1093/mnras/stz2711)
- Jurić, M., Axelrod, T., Becker, A., et al. 2019, *LSST Document LSE-163*, doi: <https://ls.st/LSE-163>
- Kelly, B. C., Bechtold, J., & Siemiginowska, A. 2009, *ApJ*, 698, 895, doi: [10.1088/0004-637X/698/1/895](https://doi.org/10.1088/0004-637X/698/1/895)
- Kim, D.-W., & Bailer-Jones, C. A. L. 2016, *A&A*, 587, A18, doi: [10.1051/0004-6361/201527188](https://doi.org/10.1051/0004-6361/201527188)
- Kim, D.-W., Protopapas, P., Bailer-Jones, C. A. L., et al. 2014, *A&A*, 566, A43, doi: [10.1051/0004-6361/201323252](https://doi.org/10.1051/0004-6361/201323252)
- Kim, D.-W., Protopapas, P., Byun, Y.-I., et al. 2011, *ApJ*, 735, 68, doi: [10.1088/0004-637X/735/2/68](https://doi.org/10.1088/0004-637X/735/2/68)
- Kluyver, T., Ragan-Kelley, B., Pérez, F., et al. 2016, in *Positioning and Power in Academic Publishing: Players, Agents and Agendas*, ed. F. Loizides & B. Schmidt, IOS Press, 87 – 90
- Komossa, S. 2015, *Journal of High Energy Astrophysics*, 7, 148, doi: [10.1016/j.jheap.2015.04.006](https://doi.org/10.1016/j.jheap.2015.04.006)
- Kovács, G., Zucker, S., & Mazeh, T. 2002, *A&A*, 391, 369, doi: [10.1051/0004-6361:20020802](https://doi.org/10.1051/0004-6361:20020802)
- Lemaître, G., Nogueira, F., & Aridas, C. K. 2017, *Journal of Machine Learning Research*, 18, 1. <http://jmlr.org/papers/v18/16-365.html>
- MacLeod, C. L., Ivezić, Ž., Kochanek, C. S., et al. 2010, *ApJ*, 721, 1014, doi: [10.1088/0004-637X/721/2/1014](https://doi.org/10.1088/0004-637X/721/2/1014)
- Mainzer, A., Bauer, J., Grav, T., et al. 2011, *ApJ*, 731, 53, doi: [10.1088/0004-637X/731/1/53](https://doi.org/10.1088/0004-637X/731/1/53)
- Martínez-Palomera, J., Förster, F., Protopapas, P., et al. 2018, *AJ*, 156, 186, doi: [10.3847/1538-3881/aadfd8](https://doi.org/10.3847/1538-3881/aadfd8)
- Masci, F. J., Laher, R. R., Rusholme, B., et al. 2019, *PASP*, 131, 018003, doi: [10.1088/1538-3873/aae8ac](https://doi.org/10.1088/1538-3873/aae8ac)
- Massaro, E., Maselli, A., Leto, C., et al. 2015, *Ap&SS*, 357, 75, doi: [10.1007/s10509-015-2254-2](https://doi.org/10.1007/s10509-015-2254-2)
- McKinney, W., et al. 2010, in *Proceedings of the 9th Python in Science Conference*, Vol. 445, Austin, TX, 51–56
- McLaughlin, M. A., Mattox, J. R., Cordes, J. M., & Thompson, D. J. 1996, *ApJ*, 473, 763, doi: [10.1086/178188](https://doi.org/10.1086/178188)
- McWhirter, P. R., Steele, I. A., Hussain, A., Al-Jumeily, D., & Vellasco, M. M. B. R. 2018, *MNRAS*, 479, 5196, doi: [10.1093/mnras/sty1823](https://doi.org/10.1093/mnras/sty1823)
- Metzger, B. D., Martínez-Pinedo, G., Darbha, S., et al. 2010, *MNRAS*, 406, 2650, doi: [10.1111/j.1365-2966.2010.16864.x](https://doi.org/10.1111/j.1365-2966.2010.16864.x)
- Mighell, K. J., & Plavchan, P. 2013, *AJ*, 145, 148, doi: [10.1088/0004-6256/145/6/148](https://doi.org/10.1088/0004-6256/145/6/148)
- Mondrik, N., Long, J. P., & Marshall, J. L. 2015, *ApJL*, 811, L34, doi: [10.1088/2041-8205/811/2/L34](https://doi.org/10.1088/2041-8205/811/2/L34)
- Mowlavi, N., Lecoœur-Taïbi, I., Lebzelter, T., et al. 2018, *A&A*, 618, A58, doi: [10.1051/0004-6361/201833366](https://doi.org/10.1051/0004-6361/201833366)
- Muthukrishna, D., Narayan, G., Mandel, K. S., Biswas, R., & Hložek, R. 2019, *PASP*, 131, 118002, doi: [10.1088/1538-3873/ab1609](https://doi.org/10.1088/1538-3873/ab1609)
- Naik, A., & Rangwala, H. 2018, *Large-Scale Hierarchical Classification with Feature Selection*, 61–74, doi: [10.1007/978-3-030-01620-3\\_4](https://doi.org/10.1007/978-3-030-01620-3_4)
- Narayan, G., Zaidi, T., Soraisam, M. D., et al. 2018, *ApJS*, 236, 9, doi: [10.3847/1538-4365/aab781](https://doi.org/10.3847/1538-4365/aab781)
- Naul, B., Bloom, J. S., Pérez, F., & van der Walt, S. 2018, *Nature Astronomy*, 2, 151, doi: [10.1038/s41550-017-0321-z](https://doi.org/10.1038/s41550-017-0321-z)
- Nun, I., Protopapas, P., Sim, B., & Chen, W. 2016, *AJ*, 152, 71, doi: [10.3847/0004-6256/152/3/71](https://doi.org/10.3847/0004-6256/152/3/71)
- Nun, I., Protopapas, P., Sim, B., et al. 2015, *ArXiv e-prints*. <https://arxiv.org/abs/1506.00010>
- Oh, K., Yi, S. K., Schawinski, K., et al. 2015, *ApJS*, 219, 1, doi: [10.1088/0067-0049/219/1/1](https://doi.org/10.1088/0067-0049/219/1/1)
- Padovani, P., Alexander, D. M., Assef, R. J., et al. 2017, *A&A Rv*, 25, 2, doi: [10.1007/s00159-017-0102-9](https://doi.org/10.1007/s00159-017-0102-9)
- Palanque-Delabrouille, N., Magneville, C., Yèche, C., et al. 2016, *A&A*, 587, A41, doi: [10.1051/0004-6361/201527392](https://doi.org/10.1051/0004-6361/201527392)

- Palaversa, L., Ivezić, Ž., Eyer, L., et al. 2013, *AJ*, 146, 101, doi: [10.1088/0004-6256/146/4/101](https://doi.org/10.1088/0004-6256/146/4/101)
- Paolillo, M., Schreier, E. J., Giacconi, R., Koekemoer, A. M., & Grogin, N. A. 2004, *ApJ*, 611, 93, doi: [10.1086/421967](https://doi.org/10.1086/421967)
- Pedregosa, F., Varoquaux, G., Gramfort, A., et al. 2012, arXiv e-prints, arXiv:1201.0490, <https://arxiv.org/abs/1201.0490>
- Peters, C. M., Richards, G. T., Myers, A. D., et al. 2015, *ApJ*, 811, 95, doi: [10.1088/0004-637X/811/2/95](https://doi.org/10.1088/0004-637X/811/2/95)
- Richards, G. T., Myers, A. D., Gray, A. G., et al. 2009, *ApJS*, 180, 67, doi: [10.1088/0067-0049/180/1/67](https://doi.org/10.1088/0067-0049/180/1/67)
- Richards, J. W., Starr, D. L., Miller, A. A., et al. 2012, *ApJS*, 203, 32, doi: [10.1088/0067-0049/203/2/32](https://doi.org/10.1088/0067-0049/203/2/32)
- Richards, J. W., Starr, D. L., Butler, N. R., et al. 2011, *ApJ*, 733, 10, doi: [10.1088/0004-637X/733/1/10](https://doi.org/10.1088/0004-637X/733/1/10)
- Rimoldini, L., Holl, B., Audard, M., et al. 2019, *A&A*, 625, A97, doi: [10.1051/0004-6361/201834616](https://doi.org/10.1051/0004-6361/201834616)
- Ritter, H., & Kolb, U. 2003, *A&A*, 404, 301, doi: [10.1051/0004-6361:20030330](https://doi.org/10.1051/0004-6361:20030330)
- Rocklin, M. 2015, in *Proceedings of the 14th Python in Science Conference*, ed. K. Huff & J. Bergstra, 130 – 136
- Rokach, L., & Maimon, O. Z. 2008, *Data mining with decision trees: theory and applications*, Vol. 69 (World scientific)
- Sánchez, P., Lira, P., Cartier, R., et al. 2017, *ApJ*, 849, 110, doi: [10.3847/1538-4357/aa9188](https://doi.org/10.3847/1538-4357/aa9188)
- Sánchez-Sáez, P., Lira, P., Mejía-Restrepo, J., et al. 2018, *ApJ*, 864, 87, doi: [10.3847/1538-4357/aad7f9](https://doi.org/10.3847/1538-4357/aad7f9)
- Sánchez-Sáez, P., Lira, P., Cartier, R., et al. 2019, *ApJS*, 242, 10, doi: [10.3847/1538-4365/ab174f](https://doi.org/10.3847/1538-4365/ab174f)
- Sarro, L., Debosscher, J., López, M., & Aerts, C. 2009, *Astronomy & Astrophysics*, 494, 739
- Sartori, L. F., Trakhtenbrot, B., Schawinski, K., et al. 2019, *ApJ*, 883, 139, doi: [10.3847/1538-4357/ab3c55](https://doi.org/10.3847/1538-4357/ab3c55)
- Schmidt, K. B., Marshall, P. J., Rix, H.-W., et al. 2010, *ApJ*, 714, 1194, doi: [10.1088/0004-637X/714/2/1194](https://doi.org/10.1088/0004-637X/714/2/1194)
- Schwarzenberg-Czerny, A. 1996, *ApJL*, 460, L107, doi: [10.1086/309985](https://doi.org/10.1086/309985)
- Silla, C. N., & Freitas, A. A. 2011, *Data Mining and Knowledge Discovery*, 22, 31, doi: [10.1007/s10618-010-0175-9](https://doi.org/10.1007/s10618-010-0175-9)
- Srivastava, N., Hinton, G., Krizhevsky, A., Sutskever, I., & Salakhutdinov, R. 2014, *Journal of Machine Learning Research*, 15, 1929, <http://jmlr.org/papers/v15/srivastava14a.html>
- Stellingwerf, R. F., & Donohoe, M. 1986, *ApJ*, 306, 183, doi: [10.1086/164331](https://doi.org/10.1086/164331)
- Tachibana, Y., & Miller, A. A. 2018, *PASP*, 130, 128001, doi: [10.1088/1538-3873/aae3d9](https://doi.org/10.1088/1538-3873/aae3d9)
- Taylor, M. B. 2005, in *Astronomical Society of the Pacific Conference Series*, Vol. 347, *Astronomical Data Analysis Software and Systems XIV*, ed. P. Shopbell, M. Britton, & R. Ebert, 29
- Udalski, A., Szymanski, M., Kaluzny, J., Kubiak, M., & Mateo, M. 1992, *AcA*, 42, 253
- van der Walt, S., Colbert, S. C., & Varoquaux, G. 2011, *Computing in Science Engineering*, 13, 22
- Van Rossum, G., & Drake Jr, F. L. 1995, *Python reference manual (Centrum voor Wiskunde en Informatica Amsterdam)*
- VanderPlas, J. T. 2018, *The Astrophysical Journal Supplement Series*, 236, 16, doi: [10.3847/1538-4365/aab766](https://doi.org/10.3847/1538-4365/aab766)
- Villar, V. A., Berger, E., Miller, G., et al. 2019a, *ApJ*, 884, 83, doi: [10.3847/1538-4357/ab418c](https://doi.org/10.3847/1538-4357/ab418c)
- . 2019b, *ApJ*, 884, 83, doi: [10.3847/1538-4357/ab418c](https://doi.org/10.3847/1538-4357/ab418c)
- Virtanen, P., Gommers, R., Oliphant, T. E., et al. 2020, *Nature Methods*, 17, 261, doi: <https://doi.org/10.1038/s41592-019-0686-2>
- Wang, C., Deng, C., & Wang, S. 2019, arXiv e-prints, arXiv:1908.01672, <https://arxiv.org/abs/1908.01672>
- Waskom, M., Botvinnik, O., O’Kane, D., et al. 2017, *mwaskom/seaborn: v0.8.1 (September 2017)*, v0.8.1, Zenodo, doi: [10.5281/zenodo.883859](https://doi.org/10.5281/zenodo.883859)
- Wenger, M., Ochsenbein, F., Egret, D., et al. 2000, *A&AS*, 143, 9, doi: [10.1051/aas:2000332](https://doi.org/10.1051/aas:2000332)
- Woosley, S. E., Heger, A., & Weaver, T. A. 2002, *Reviews of Modern Physics*, 74, 1015, doi: [10.1103/RevModPhys.74.1015](https://doi.org/10.1103/RevModPhys.74.1015)
- Wright, E. L., Eisenhardt, P. R. M., Mainzer, A. K., et al. 2010, *AJ*, 140, 1868, doi: [10.1088/0004-6256/140/6/1868](https://doi.org/10.1088/0004-6256/140/6/1868)
- Zaharia, M., Xin, R. S., Wendell, P., et al. 2016, *Communications of the ACM*, 59, 56
- Zorich, L., Pichara, K., & Protopapas, P. 2020, *MNRAS*, 492, 2897, doi: [10.1093/mnras/stz3426](https://doi.org/10.1093/mnras/stz3426)